TAMPERE UNIVERSITY OF TECHNOLOGY

Ahmad Mardoukhi

High Temperature High Strain Rate Behavior of Superalloy MA 760

Master's thesis

Examiners: Professor Veli-Tapani Kuokkala and Research Fellow Mikko Hokka

Examiners and topic approved by the

Faculty Council of the Faculty of

Engineering Sciences on 6 March 2013

Contents

PREFACE

This project was carried out at the Department of Materials Science of Tampere University of Technology during the years 2012-2013. To Dr. Mikko Hokka, I am deeply grateful for an interesting research subject, and I want to express my sincere appreciation to him for his continued support, encouragement, and valuable advices during the course of the work. I am also most grateful to Professor Veli-Tapani Kuokkala to give the opportunity to work in an inspiring group.

Dr. Matti Isakov deserves my special gratitude for his elaborate assistance in constructing the high temperature apparatus for the Taylor impact test. Mr. Dmitri Gomon is greatly acknowledged for his help in carrying out the Split Hopkinson Pressure bar tests. Mr. Ari Varttila deserves my special thanks for helping with designing and building the high temperature apparatus for the Taylor impact test.

To the staff and colleagues at the Department of Materials Science, I wish to express my special appreciation for creating friendly environment, in which it has been a pleasure to carry out these studies.

I am really grateful for the support of my friends, Aiat, Daniele, Francesco and Amira within this time.

Finally I wish to thank my family, my brother Yousof and my parents, Masoud and Mitra for their support during my studies.

Tampere, Finland

October 2013 Ahmad Mardoukhi

ABSTRACT

The objective of this work was to investigate the high strain rate and high temperature behavior of mechanically alloyed and oxide dispersion strengthened nickel based superalloy MA 760. These types of alloys are used in many high temperature applications, such as turbine blades, where also impact type loadings can occur. Therefore, understanding the behavior of the alloy at its operating temperatures can help designing better and safer components in the cases of high rate impacts and collisions.

The high strain rate high temperature tests were carried out using the Split Hopkinson Pressure Bar device at different strain rates and temperatures. The tests were carried out at strain rates between 1050 s^{-1} and 3800 s^{-1} and at temperatures ranging from room temperature up to 900 ^{o}C. The obtained data was analyzed based on the principles of the Split Hopkinson Pressure Bar, focusing on the yield strength, strain rate, and fracture strain.

Based on the test results, the effects of strain rate and temperature on the mechanical behavior of the MA 760 was described. Yield strength increases as a function of temperature until temperatures close to 700^{o}C, after which the yield strength decreases. However, even after this decrease the material is still very strong, which makes this material suitable for high temperature applications. The reason for this observed behavior is the anomalous yielding behavior of the γ' phase. The flow stress increases with increasing temperature until the maximum. At higher temperatures (above 700 ^{o}C), the deformation starts in the γ matrix, which causes the reduction in the yield strength of the material. Around 900 ^{o}C, the initial cuboidal microstructure changes its morphology, which leads to the further reduction of the strength of the material.

During the work of this thesis, a high temperature apparatus for the Taylor impact test was designed and built. The apparatus consists of the sample holder made of Teflon. The sample is placed in the sample holder with a ceramic wool ring. Two thermocouples are attached to each end of the specimen to monitor the temperature of the specimen. A stopper filled with ceramic wool was built to catch the specimen and the projectile. An induction heater was used to heat up the specimen to the test temperature. The impact process was recorded with a high speed camera to measure the speed of the projectile. The device was successfully tested and the results obtained from the tests were comparable with literature and the result obtained from the Split Hokinson Pressure Bar.

ABBREVIATION AND SYMBOLS

A	Cross section of the bars
A	Cross section at the point where the material in the Taylor test is brought to rest
A_0	Cross section of the projectile before plastic deformation
a	Lattice constant
b	Burgers vector
c	Concentration of solute atoms
c	Velocity of the elastic wave
C_b	Longitudinal wave speed in the bar
d	Grain diameter
DSP	Departure side pinning
e	Longitudinal strain caused by the compression
f	Volume fraction of precipitated second phase
f	Functions describing the incident wave
fps	Frames per second
G	Shear modulus
g	Functions describing the reflected wave
GAR	Grain aspect ratio
G_{mix}	Free energy of mixture
h	Functions describing the transmitted wave
k	Boltzmann's constant
k_y	Measures the relative hardening contribution of grain boundaries
l	Distance between two precipitates
$\bar{l}$	Mean free dislocation spacing
M	Present metallic elements
MA	Mechanical alloying
MRS	Mean rate of strain
m_a	Number of atoms per powder particle of element A
$\bar{M}$	Average orientation factor
n	Number of dislocations in the pile up
N_a	Avogadro's number
ODS	Oxide dispersion strengthening
Q	Activation energy
R	Gas constant
r	Particle radius
R_P	Yield strength in the loading direction
S	Configurational entropy
S	Area of the surface of a particle
S_T	The total surface area of n_i isolated particles
T	Temperature
T	Duration of the impact
t	Time
T_m	Melting temperature
T_R	Recrystallization temperature
U	Velocity of impact
u_1	Displacements in the incident bar
u_2	Displacements in the transmitter bar
u_i	Incident displacement
u_r	Reflected displacement
u_t	Transmitted displacement
V_i	Volume of a particle

V_m	Molar volume
v	Velocity of the plastic boundary
w	Number of configurations
x	Molar fraction
x	The part of the specimen without plastic deformation
z	Coordination number
γ	Continuous austenitic phase with FCC structure
γ’	Main precipitate phase
δ	Size misfit parameter
δ	Thickness of the grain boundary
ΔH_m	Molar enthalpy of mixing
ΔS_M	Molar entropy of mixing
$\Delta\varepsilon$	Change in the strain with time
$\Delta\tau$	Shear stress needed to overcome the dislocation barrier
ε	Misfit strain
ε_{AA}	Binding energy of a pair of A atoms
ε_{eng}	Engineering strain
ε_{true}	True strain
$\dot{\varepsilon}$	Strain rate
η	Modulus misfit parameter for the shear modulus
θ_I	Strain hardening rate
K	Bulk modulus
λ	Angle between the slip direction and the tensile axis
μ^o	Free molar energy
ρ	Dislocation density
ρ	Density of the material
τ	Shear stress
σ_{eng}	Engineering stress
σ_i	Overall resistance of the lattice to dislocation motion
σ_{true}	True stress
σ_y	Yield strength of polycrystalline material
τ_C	Critical resolved shear stress
τ_s	Average resolved shear stress in the pile-up plane
Φ_i	Volume of an atom
Φ	Angle between the normal of the slip plane and the tensile axis
χ	Modulus misfit parameter for the bulk modulus
Ω	Regular solution paramete

1. INTRODUCTION

Strong need exists to develop new and better materials. Obtaining better properties at higher temperatures and at more aggressive environments are examples of these needs. Modifications of composition of the existing materials as well as new processing techniques are being developed for better performance. Superalloys' development is usually associated with the hot parts of turbine engines, but similarly, better alloys are also needed in other applications, such as components of the petrochemical industry as well. Failure of material in these applications may not be as drastic as the failure of an airplane engine. However, the demand for economic and reliable performance has been a great motivation for the development of better materials in these fields of industry. One of the most promising groups of materials are the ODS superalloys, which have had a continuously increasing number of applications during the recent years.

As recently a large number of new commercial materials and materials in the development stage have entered the market, the need for understanding their behavior, such as mechanical behavior and deformation mechanisms, has increased rapidly. In addition, there is a need to predict the long term properties and durability of these materials under the mechanical and thermal stresses. All of these requirements have directed the research of high temperature materials. However, understanding the mechanical properties, such as tensile, creep, and fatigue, of even one material requires a lot of scientific work.

Recently, different aspects of fatigue, creep, and corrosion properties of these types of materials have been studied widely, but less attention has been paid to their properties at high strain rates and at high temperatures. It should be noted that there are numbers of different variables affecting the material behavior at high temperatures thus making the interpretation of the tests results more difficult. Concluding all of this, the significance of studying the behavior of MA 760 at high strain rates and at high temperatures becomes apparent.

The present work starts with a literature review. At first the description of the microstructure of the nickel based superalloy is presented. Then a detailed description of the mechanical alloying process and mechanisms of strengthening of ODS alloys followed by the description of the high temperature behavior of nickel based superalloys will be presented as well. Then the theoretical part of the testing method is presented, and finally the procedure for carrying out the tests followed by the results of the mechanical tests on MA760 at different conditions are presented and discussed.

The basis of the experimental part is related to the Split Hopkinson Pressure Bar and Taylor impact tests. In the room temperature, the strain rate was varied in the Split Hopkinson Pressure Bar tests, whereas at the high temperature tests the strain rate was kept constant as the temperature changed (500^{o}C, 800^{o}C, and 900^{o}C). For the Taylor impact tests, the main focus was aimed at designing and building the high temperature test apparatus and using of in tests to show the capabilities of the device.

2. Nickel based superalloys

Nickel based superalloys are specially designed to resist high temperatures, and to have the ability to keep their strength at high temperatures. These complex alloys also have good resistance to corrosion, oxidation creep, and failure even at high temperatures. (1 p. 511)

2.1 Chemical composition and special applications

The first nickel based superalloy with precipitation hardening ability, Nimonic 80, was designed in the United Kingdom in 1941. Basically this alloy is a solid solution of nickel with 20%Cr, 2.25%Ti, and 1%Al. The purpose of the alloying is to produce $Ni_3(Al,Ti)$ precipitates. During the years, this superalloy has been further developed by adding Mo, Co, Nb, Zr, B, Fe, and other alloying elements. Nowadays around a hundred different nickel based superalloys are being produced for various industrial applications. The most important fields of application for these are the aerospace and power generation industries. In addition, nickel based superalloys are being used in submarines, petrochemical industry, and in various other high temperature applications. (1 p. 511)

2.2 Microstructure

Figure 1 shows the general microstructure development of the nickel based superalloys. The improvement of the mechanical properties is due to the solid solution and precipitation hardening, as well as the optimal distribution of carbides. The main phases of the nickel based superalloys are:

- γ Phase: Uniform austenitic matrix with FCC structure
- γ' Phase: Main precipitation phase
- Carbides: Normally $M_{23}C_6$ and MC, where M presents a metal.
- Oxide dispersions (such as $Y_2O_{3)}$ (1 p. 513) (2 pp. 3261-3266)

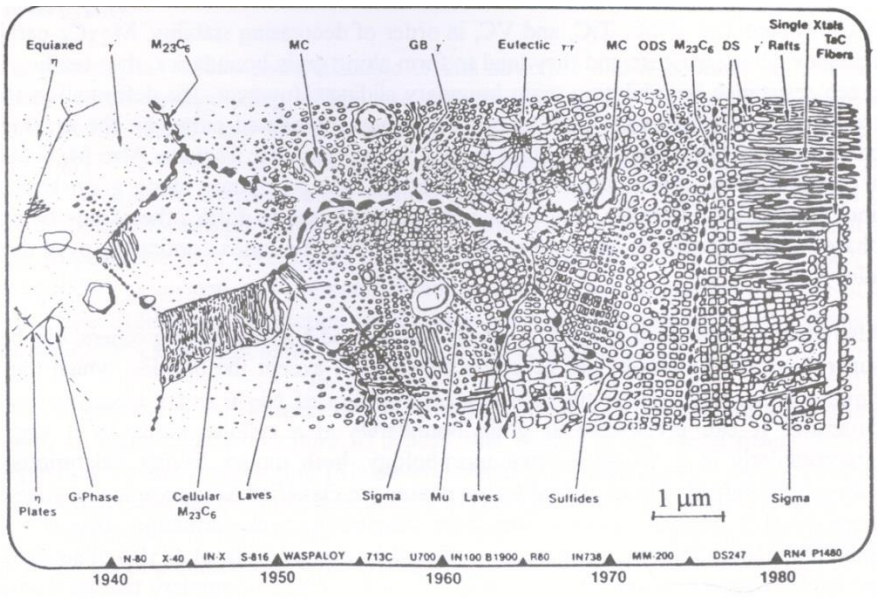

Figure 1 Development of the microstructures in nickel based superalloys (1 p. 514)

During the development years of the nickel based superalloys (1940-1970), there are some changes in microstructure, which are notable to mention:

- Volume fraction of γ' has increased.
- Size of γ' increased at first, but later it was kept around 1 μm.
- γ' structure became more similar to a cubic structure.
- Second precipitates of γ' with low distance from each other started to appear.

During these developments, some of the nickel based superalloys showed structural problems. One of these problems is related to the cellular carbides, such as $M_{23}C_6$carbides and the σ-phase. These cellular carbides lead to low fracture life at high temperatures, and the σ-phase can cause low temperature brittleness. In addition, the σ-phase may lead to brittleness at low temperatures and/or low fracture life time as well. The problems caused by the cell structured carbides can be fixed by proper heat treatments, and the problems caused by the σ-phase can be solved by making some changes in the chemical composition. (1 p. 513)

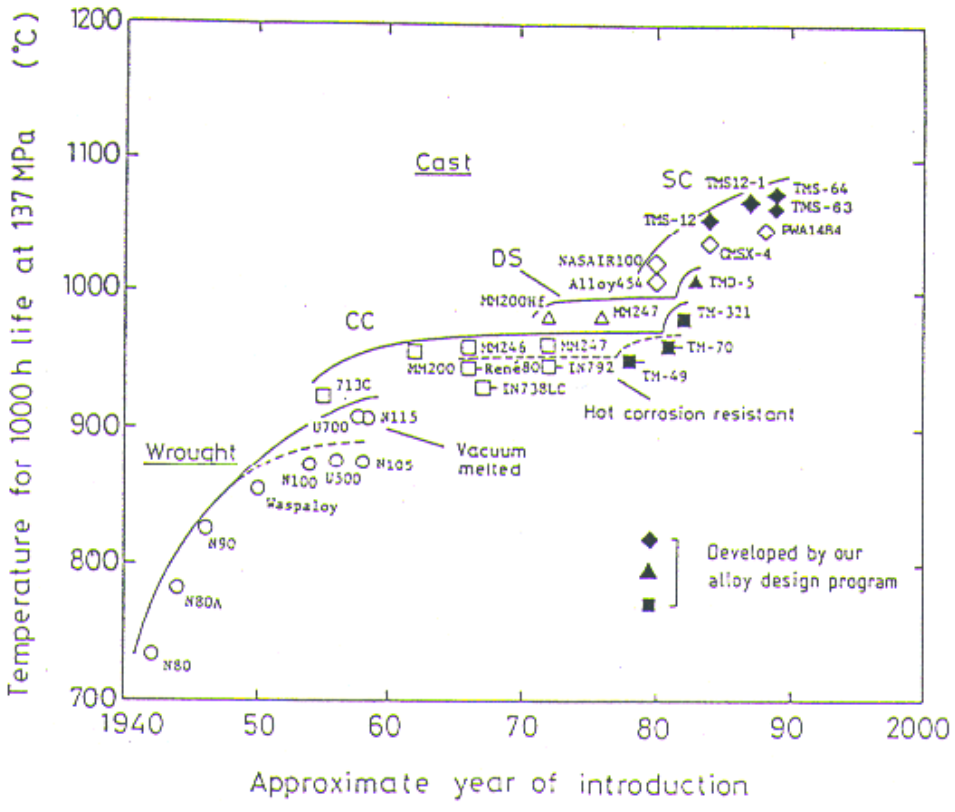

Figure 2 The development of superalloys (3)

2.2.1 γ-Phase

The γ-phase is the uniform austenitic matrix of the nickel based superalloys. This phase gains more strength by increasing the amount of alloying elements, such as Cr, Mo, W, Co, Fe, Ti, and Al. The difference between the atomic diameters of these elements with Ni is between 1% and 13%. Aluminum increases the strength by two different mechanisms: firstly by producing precipitates, and secondly by solid solution strengthening. W, Mo, and Cr increase the strength by solid solution strengthening as well.

At temperatures above $0.6T_m$, where creep mechanisms are active, the increase in strength depends on diffusion. Tungsten and molybdenum are alloying elements, which have a low diffusion rate. These two elements have the strongest impact on reducing the creep rates at high temperatures. Cobalt reduces the stacking fault energy and increases the distance between partial dislocations and, therefore, makes the cross slip more difficult. As a result the high temperature stability of these superalloys increases. (1 pp. 513-516)

2.2.2 γ' Phase

γ'-phase forms in the austenitic nickel based superalloys as a result of the precipitation hardening heat treatment. γ' precipitates in the matrix with high nickel content have an FCC structure, and its chemical composition is A_3B. "A" is an element with rather high electronegativity, such as Ni, Co, Fe, or B compared to more electropositive elements, such as Al, Ti, and Nb. Normally in the nickel based superalloys, the γ' phase has a chemical composition of $Ni_3(Al,Ti)$. In the case of cobalt alloying, the cobalt takes the place of some of the nickel atoms and the chemical composition of the precipitates will be $(Ni,Co)_3(Al,Ti)$. (1 pp. 516-517)

2.2.3 Carbides

The amount of carbon in the nickel based superalloys usually varies between 0.02% and 0.6%. Metallic carbides are formed both inside the grains and on the grain boundaries. Since the carbides are typically more brittle and harder than the matrix of the superalloy, the distribution of carbides on the grain boundaries has a strong impact on the high temperature strength, formability, and overall creep behavior. If there are no carbides along the grain boundaries, voids join together and dislocation slip happens at the grain boundaries during high temperature deformation. On the other hand, continuous chains of carbides at the grain boundaries can lead to low fracture toughness. The optimal properties can be obtained when series of non-continuous chains of carbides are formed at the grain boundaries. These non-continuous carbides prevent the initiation and propagation of transgranular cracks.

The most typical carbides found in nickel based superalloys are MC, $M_{23}C_6$, and M_6C. MC carbides are considered as mono-carbides. "M" can be replaced by a metallic element, such as Ti, Ta, Nb, or W. MC carbides are completely stable, and they appear just below the solidification temperature. During the solution treatments, it is almost impossible to dissolve these carbides. Also, these carbides prevent grain growth during solution treatment.

In $M_{23}C_6$ carbides, “M” is usually chromium, but can also be iron in some rare situations depending on the type of the superalloy. Also tungsten, molybdenum, and cobalt are sometimes found to form such carbides. These carbides form in different situations, such as during heat treatments in the temperature range of 815 ^{o}C to 980 ^{o}C and during cold working. $M_{23}C_6$ carbides can be formed from decomposition of MC carbides or directly from the free carbon, and it normally deposits along the grain boundaries.

M_6C carbides form in the temperature range of 815^{o}C to 980^{o}C, and they are similar to $M_{23}C_6$ carbides. The tendency to form M_6C carbides increases when the amount of molybdenum and tungsten is rather high. M_6C carbides have a complex cubic structure, and when the amount of molybdenum or tungsten is more than 6-8%, the M_6C carbides start to form along the grain boundaries with the $M_{23}C_6$ carbides. (1 pp. 517-519)

2.2.4 Oxide dispersion

Oxide particles play a major role in the oxide dispersion strengthened (ODS) alloys. The characteristics of the oxide particles are different in each alloy. The volume fractions of the oxide particles can vary from 1.0% to 3.0%. Also the diameters of these particles vary roughly from 14 nm to 32 nm depending on the alloy. As an example Y_3Al_5O12, $YAlO_3$ and $Y_4Al_2O_9$ particles can be found in MA6000 alloy. (2) (3)

3. ODS superalloys

Oxide dispersion-strengthened (ODS) materials are specially designed mechanically alloyed metals for high temperature applications. Heat treatments are always necessary for ODS materials. Mechanical alloying itself is a complicated process to carry out, and most of the alloys produced using this method are heterogeneous. Therefore, heat treatments are needed to obtain a uniform and reproducible microstructure with controlled recrystallization of grain structure. (4) The first attempt to produce an ODS alloy was the manufacturing of “ductile tungsten” using powder metallurgy in 1910. Although this method was not very useful in the production of large components or large numbers, it was the starting point in the history of ODS alloys. Also it is notable that in those days, the theoretical understanding of the mechanisms, which occur in ODS alloys was quite poor. A great achievement in the manufacturing of ODS alloys took place in 1930 by applying internal oxidation of powders to cobalt-silver and beryllium alloys as well as sintering of aluminum powders. However, the procedure could not be applied to every alloy. The biggest problems were the costs and the fact that only a few alloying elements could be added. Later on, these problems were solved by mechanical alloying (MA), and this procedure was successfully used to produce nickel- and iron based superalloys. (3)

3.1 Mechanical alloying

Mechanical alloying is a process, which is carried out in the solid state. The process includes repeated welding, fracturing, and rewelding of powder particles by high-energy ball milling. This method was originally developed to manufacture ODS nickel- and iron-based superalloys for aerospace industry. (5) (6)

In principle, any alloy can be produced by deforming the mixture of different powders. The high-energy ball milling produces heterogeneous mixtures of powders and turns them into a solid solution with fine grain structure. The oxide particles are dispersed into the solid solution. Both ambient and elevated temperature strength are increased by these oxide particles. The mechanically-alloyed powders are normally compacted and extruded at a high temperature or hot-rolled to increase the density of the material, as well as to give the material shape (Fig.3) (4) (5)

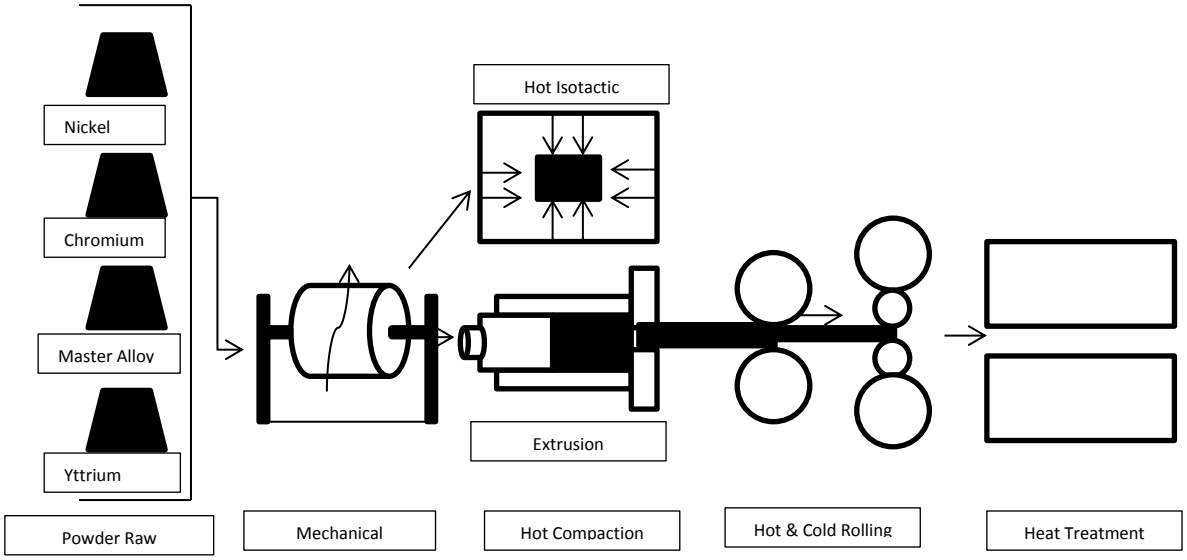

Figure 3 A general process for the manufacturing of mechanically alloyed metals. (5)

The process consists of several steps including heat treatments to recrystallize the alloy. By choosing the correct heat treatment, the microstructure can be designed either to resist creep or low temperature deformation. A coarse columnar grain structure resists creep at high temperatures, whereas fine equiaxed grains work better at ambient temperature applications. There are two main classes of commercial ODS alloys, iron based and nickel based alloys. The compositions of some typical alloys are shown in Table1. (5)

Table 1 Compositions (wt. %) of some common superalloys. MA758 and PM1000 are nickel based alloys without γ' strengthening. (5)

Fe-based	C	Cr	Al	Mo	Ti	N	Ti_2O_3	Y_2O_3	Fe
MA957	0.01	14.0	-	0.3	1.0	0.012	-	0.27	Balance
DT2203Y05		13.0	-	1.5	2.2		-	0.5	Balance
ODM331		13.0	3.0	1.5	0.6		-	0.5	Balance
ODM751		16.0	4.5	1.5	0.6		-	0.5	Balance
ODM061		20.0	6.0	1.5	0.6		-	0.5	Balance
MA956	0.01	20.0	4.5	-	0.5	0.045	-	0.5	Balance
PM2000	<0.04	20.0	5.5		0.5		-	0.5	Balance
PM2010	<0.04	20.0	5.5		0.5		-	1.0	Balance
DT		13.0	-	1.5	2.9		1.8	-	Balance
DY		13.0	-	1.5	2.2		0.9	0.5	Balance

Ni-based	C	Cr	Al	Ti	W	Fe	N	Total O	Y_2O_3	Ni
MA6000	0.06	15.0	4.5	2.3	3.9	1.5	0.2	0.57	1.1	Balance
MA760	0.06	19.5	6.0	-	3.4	1.2	0.2	0.6	1.0	Balance
MA758	0.05	30.0	0.3	-	0.5	-	-	0.37	0.6	Balance
PM1000		20.0	0.3	0.5		3.0			0.6	Balance

3.2 Thermodynamics of mechanical alloying

Consider pure components A and B with molar free energies of μ°_A and μ°_B. The average free energy of the mixture of these two components in the powder form is given by:

$$G_{mix} = (1-x)\mu^0{}_A + x\,\mu^0{}_B \quad (1)$$

where x is the molar fraction of B. Suppose that the A and B powder particles consist only of A or B atoms, and the particles are so large that the atoms of each component do not feel the unlike atoms by interatomic bonding. If there are only few different ways to rearrange the mixture of the powder particles, these rearrangements do not have a notable contribution to configurational entropy of mixing. Therefore, the mixture of the powders that follows the above Equation is called a mechanical mixture. (7)

On the other hand, a solution is a mixture of atoms or molecules. Therefore, the enthalpy will also change as the near-neighbor atomic and/or molecular bonds change because the total number of ways that the particles can rearrange is very large. For example, consider a molecule of CH_2N_2. The carbon atom has four covalent bonds with the other atoms that can change their place within the molecule without changing the composition. The configurational entropy changes as well because the particles can rearrange in many different ways. Therefore, the free energy of the solution is different from the mechanical mixture. Normally, the solid solutions do not form from the mixture of large particles as it happens in mechanical alloying. Instead, the particles go through different transitions, such as decreasing the particle size. This is the process, which happens in mechanical alloying. In order to analyze the thermodynamics of the solid solution formation in mechanical alloying, consider a binary system of pure components of A and B. The Equation for the free energy of mixing in this

situation contains particle sizes that can be greater than an atom. This is in contrast to the conventional approach to the solution theory. (7)

3.2.1 Configurational Entropy

The change in the configurational entropy can be calculated using the Boltzmann Equation:

$$S = k\,Ln(w) \tag{2}$$

where k is the Boltzmann's constant and w is the number of configurations. When the powders are mixed randomly, the number of possible configuration can be calculated using the following Equation:

$$\frac{(\mathrm{N_a}([1-\mathrm{x}])/(\mathrm{m_B}+\mathrm{x}/\mathrm{m_A}))!}{\left(\frac{N_a[1-x]}{m_a}\right)!\left(\frac{N_a x}{m_B}\right)} \tag{3}$$

where m_a and m_B are the number of atoms per powder particle of element A and B, respectively. x is the mole fraction of B, and N_a is Avogadro's number. By using the Stirling's approximation and assuming that the number of particles remains integral and non-zero, the molar entropy of mixing can be calculated as follow:

$$\Delta S_M = -kN_a\,[(1-x)\,Ln\,(1-x) + xLn\,(x)] \tag{4}$$

Obviously, the largest reduction in free energy occurs when the particle sizes are atomic as it can be seen in Figure 4. This Figure shows that the entropy of mixing cannot be ignored when the particle size is less than a few hundred atoms. (7)

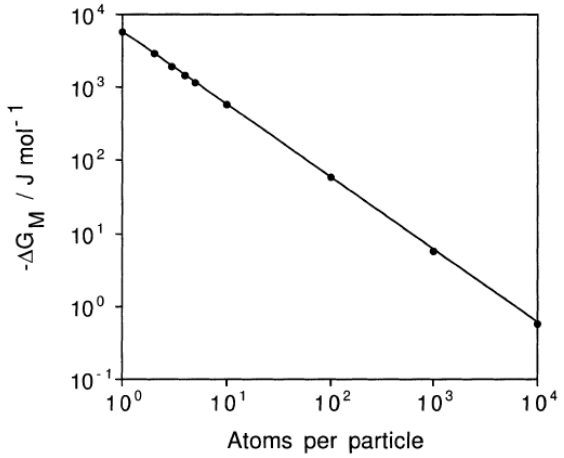

Figure 4 Molar Gibbs free energy of mixing for a binary alloy as a function of particle size when all the particles are of uniform size. (7)

3.2.2 Enthalpy

The major part of the enthalpy of mixing comes from the change in the energy when new bonds are formed during the formation of the solid solution. In the regular solution models, the enthalpy of mixing is calculated from the energy of the bonds of the different kinds of near-neighbor particles. This information gives the required change in the enthalpy on mixing. The binding energies can be defined as the change in the energy as the distance between a

pair of atoms move from infinite distance to their equilibrium distance. If the binding energy of a pair of A atoms is ε_{AA}, then atoms prefer to be neighbors to their own kind if $\varepsilon_{AA} + \varepsilon_{BB} > 2\varepsilon_{AB}$ and vice versa. With the approximation that the atoms in the solid solution are randomly distributed, the number of A-A bonds in a mole of solution is $zN_a(1-x)^2$, B-B bonds zN_ax^2, and A-B bonds $2zN_a(1-x)x$, where z is the coordination number. Then the molar enthalpy of mixing can be calculated using:

$$\Delta H_m = N_a\, z(1-x)\, xw \tag{5}$$

$$w = \varepsilon_{AA} + \varepsilon_{BB} - 2\varepsilon_{AB} \tag{6}$$

where Z is the coordination number, x is the mole fraction of B, and w is equal to $\varepsilon_{AA} + \varepsilon_{BB} - 2\varepsilon_{AB}$. The term zN_aw is called the regular solution parameter (Ω). (7)

These rules are applicable to particles, such as those atoms, which feel the influence of unlike atoms. For example the atoms, which are at the interface of A and B particles. For a cubic particle the surface, S, can be calculated using:

$$S = 6(V_i)^{2/3} \tag{7}$$

$$V_i = m_i\ \Phi_i \tag{8}$$

$$V_T = \sum_I \left(N_a \frac{x_i}{m_i}\right) V_i \tag{9}$$

where V_i is the volume of each particle, subscript i represent the component, Φ_i is the volume per atom, N_a is Avogadro number, and x_i is the mole fraction. The total surface area of n_i isolated particles is:

$$S_T = \sum_i n_i S \tag{10}$$

When the particles are compacted, the total grain boundary area is half of this value, which can be calculated using:

$$S_V = \left(\frac{1}{2} \sum_I n_i 6(m_i\, \Phi_i)^{2/3}\right) / \left(\sum_I \left(\frac{N_a\, x_v}{m_i}\right) V_i\right) \tag{11}$$

The enthalpy of mixing can be generated only in the region where unlike atoms meet.

$$\Delta H_m = \Omega\, \delta\, S_V\, x(1-x) \tag{12}$$

where δ is the thickness of the grain boundary. (7)

3.2.3 Interfacial energy

The role of the interface is to define the number of atoms, which can interact with atoms on the surfaces of other particles. One aspect, which has to be taken into account, is the presence of disordering at and near the interface, which causes the interfacial energy σ per unit area. This term is not included in the theory of conventional solutions. The chemical component of interfacial energy already exists in the enthalpy of mixing, but this term can be calculated separately using the following Equation:

$$\Delta H_I = V_m S_V \sigma \quad (13)$$

where V_m is the molar volume. ΔH_I is the change in the enthalpy, caused by the interfaces. It is supposed that V_m is almost zero for very large particles. In mechanical alloying the process goes towards producing smaller particles to form the solid solution. Additionally, it is supposed that the interfacial energy per unit area (or σ) is different for A-A particles, B-B particles, and A-B particles. (7)

Figure 5 shows the results of modeling of the atomic solution for the particles with one atom in size. It is worth mentioning that the mixing energy of pure components is zero. Three cases for the solutions are shown in Figure 5; the atoms tend to cluster (Ω>0), tend to order (Ω<0), or form the ideal solution (Ω=0). Interfacial energy does not appear in these diagrams as the solution is atomic and completely coherent.

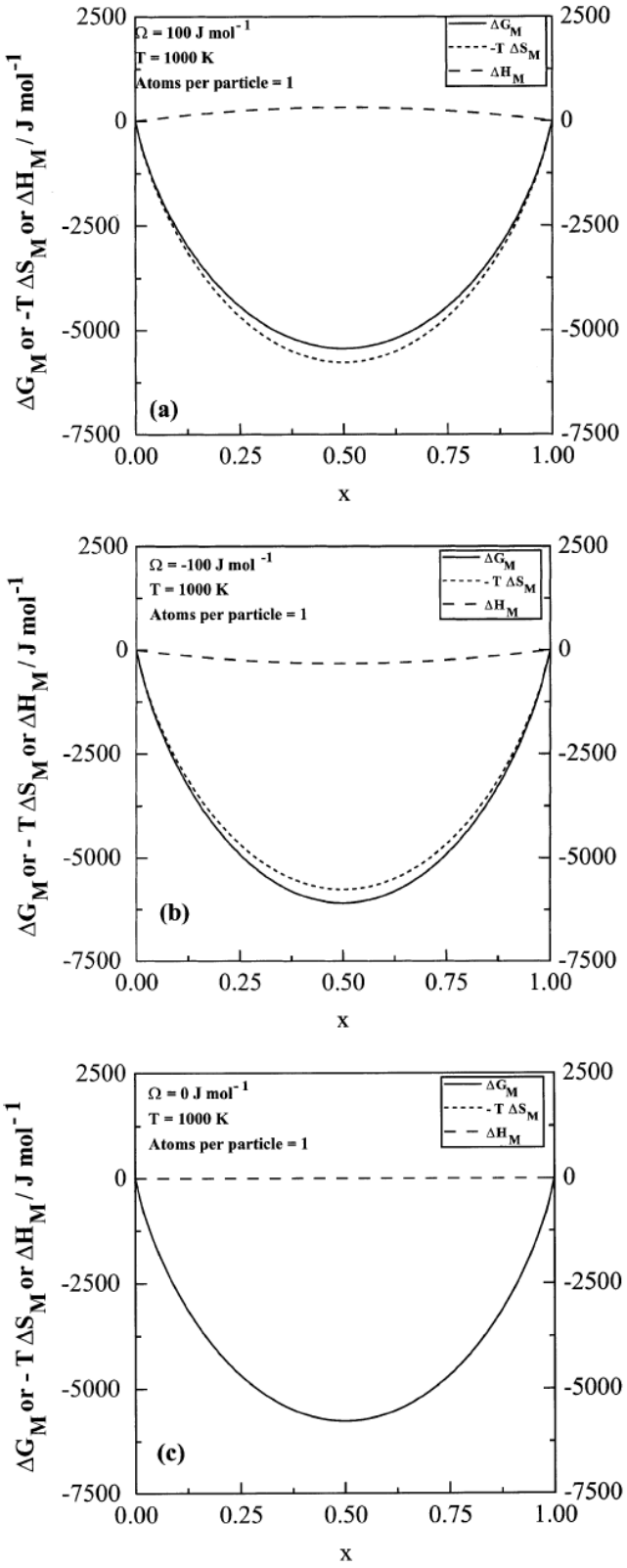

Figure 5 Free energy, entropy, and enthalpy of mixing of a binary system at 1000K (7)

During mechanical alloying, component powders are fractured and deformed repeatedly until an atomic solid solution is formed. This refinement of particle size increases the amount of interface per unit volume (S_V). If the interface energy is constant, the amount of energy, according to Equation (13), must suppress any advantage of entropy and enthalpy of mixing. Thus, the mechanical alloying cannot take place unless there is a gain in coherency. This coherency is gained by reducing the particle size to the atomic dimensions, which reduces the interfacial energy. As the change in the interfacial energy with the change in particle size in not known, assume that the interfacial energy per unit area, σ, remains constant until the particles size reaches 10^7 atoms. After this the interfacial energy decreases linearly to zero as the particle size reaches 1 atom. The results are shown in Figure 6.

The free energy in mechanical alloying starts to change as the particle size reduces to 10^9 atoms. The main contribution in the change of the free energy is the increase in the interfacial energy component. The net free energy remains positive until the contribution of the entropy of mixing and enthalpy become significant. Figure 7 shows the barriers for the formation of a solid solution in the mechanical alloying process. This Figure shows that the barriers can occur because of the supplementation of interfacial energy. This dominates in the early stages until the particle size reaches the value where coherency is gained. (7)

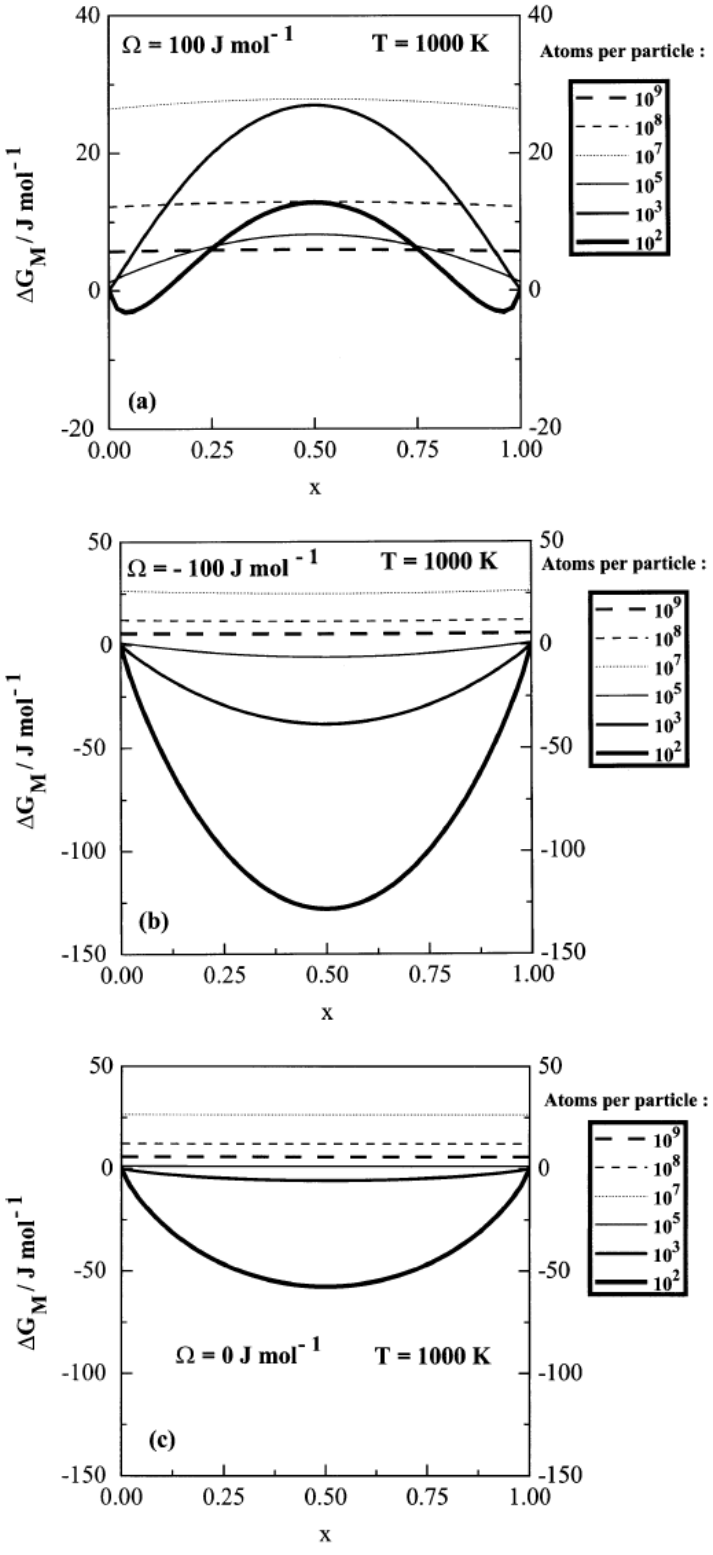

Figure 6 Free energy of mixing of a binary system at 1000K as the function of number of atoms per particle (7)

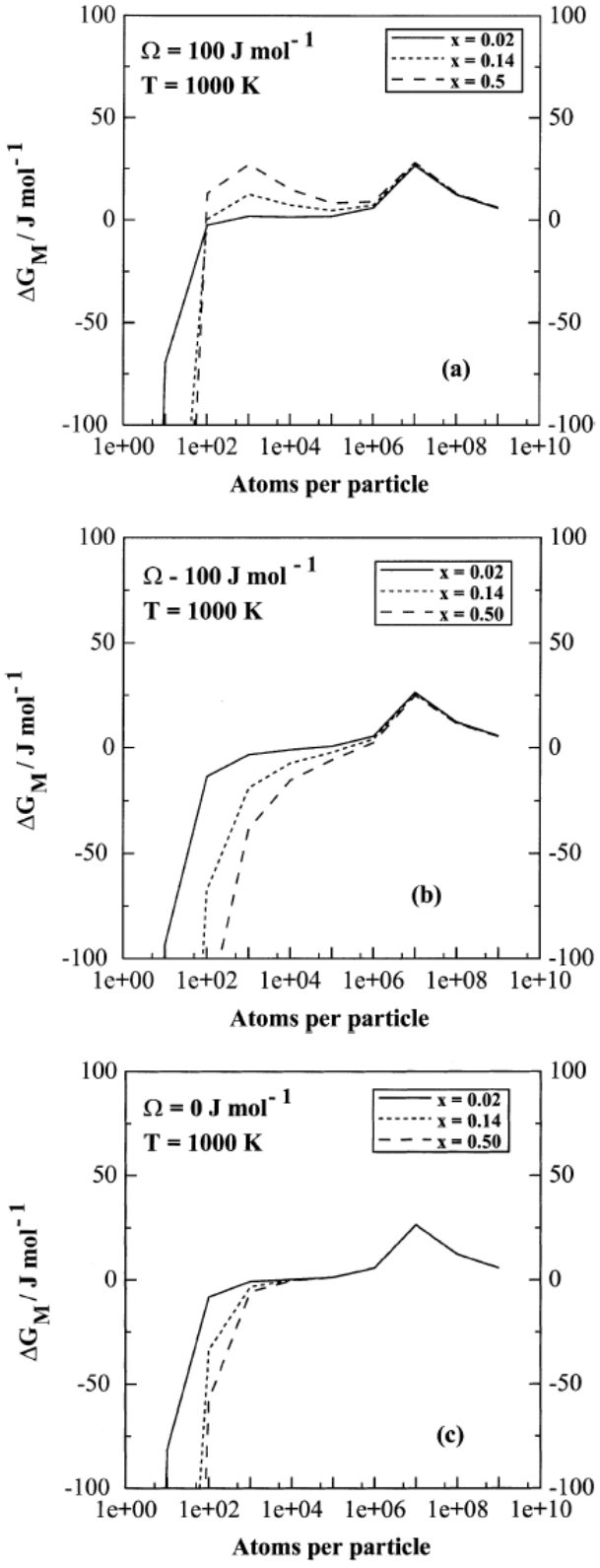

Figure 7 Free energy as a function of the number of atoms per particle and at different concentrations (7)

3.3 Solution formation during mechanical alloying

The solid solution is produced by mixing the solid aggregates of the components, which can contain millions of identical atoms. Badmos and Bhadeshia (7) analyzed the procedure, in which the atomic solution is produced from these aggregates. The size scale, where the mixture of particles starts to show solution-like behavior, is important. This scale size can be easily calculated in the case where there is no enthalpy of mixing. Therefore, just by calculating the configurational entropy of the mixture it is possible to estimate at which point the mixture starts to behave as a solution. In reality, however, there are no ideal solutions for cases where the enthalpy of mixing is zero. The enthalpy can be calculated using the solution theory. However, some modifications are needed since in the mechanical alloying the interacting atoms see each other only at the interfaces between the particles, and the enthalpy of mixing is only due to the atoms, which are located at the interfaces. This is the chemical component of the interfacial energy. The structural components, such as the misfit dislocations, oppose the mechanical alloying. This is due to the increasing interfacial area per unit volume. Therefore, it is predicted that the formation of an atomic solution does not take place since the tendency towards the mixing becomes lower as the cost of creating interfaces grows as the particles size become smaller. Yet the experiments by Badmos and Badeshia (7) show that the mixing does happen. This conflict can be explained by considering the increase in coherency as the particle size becomes smaller and smaller during the mechanical alloying. The mechanism is shown in Figure 8, which illustrates how the structural component decreases as the particle size decreases (5). This is completely opposite to that what happens in the formation of precipitates in the solid-state. At first, the precipitates are coherent, and then start to lose their coherency as they grow bigger. Consequently, during the formation of the solution in mechanical alloying, the particles need to gain coherency. (5)

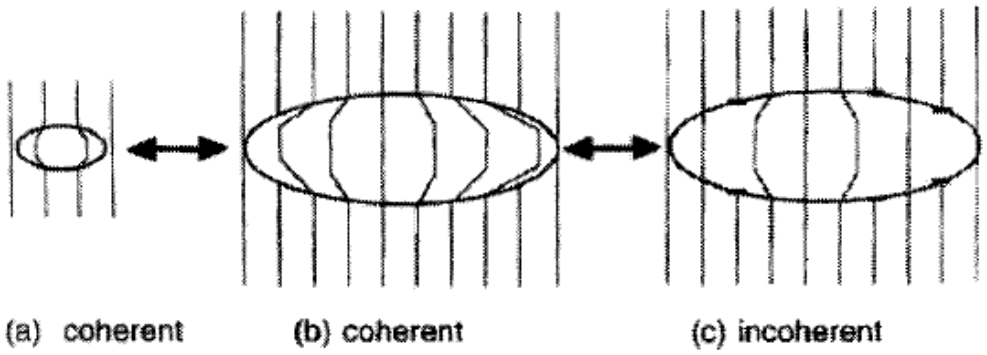

Figure 8 Change in the coherency as a function of particle size. The lines represent the lattice planes. (5)

When an atomic solution has been achieved, the chemical component of the interfacial energy of the mechanical solution equals the solution enthalpy of mixing of an atomic solution. Positive enthalpy of mixing opposes the formation of solid solution and vice versa. The structural component always opposes the mixing unless the reducing of the particle size leads to the decreasing of interfacial energy. As the consequence of these conflicts, there will be several barriers to the formation of the solid solution, as shown in Figure 9. (5)

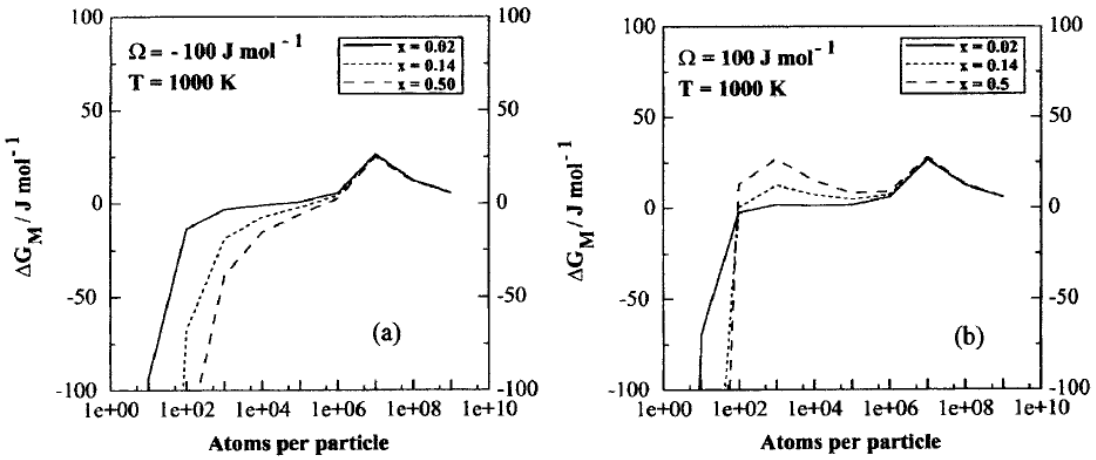

Figure 9 Thermodynamic barriers to the formation of a solid solution a) enthalpy of mixing is negative, and b) positive enthalpy of mixing, tendency to cluster. (5)

3.4 Initial microstructure

The grain size can be as fine as 1-2 nm locally after the mechanical alloying process. The consolidation temperature is about 1000 °C, and the process typically includes hot extrusion and rolling, which lead to recrystallization into sub-micrometer grain sizes (Fig. 10a).The recrystallization may occur several times during the consolidation process. The sub-micrometer grains are not simply miss-oriented dislocation cells, but real grains with considerable miss-orientation angles between adjacent grains. Consecutive heat treatments can lead to a very coarse grained microstructure. (5)

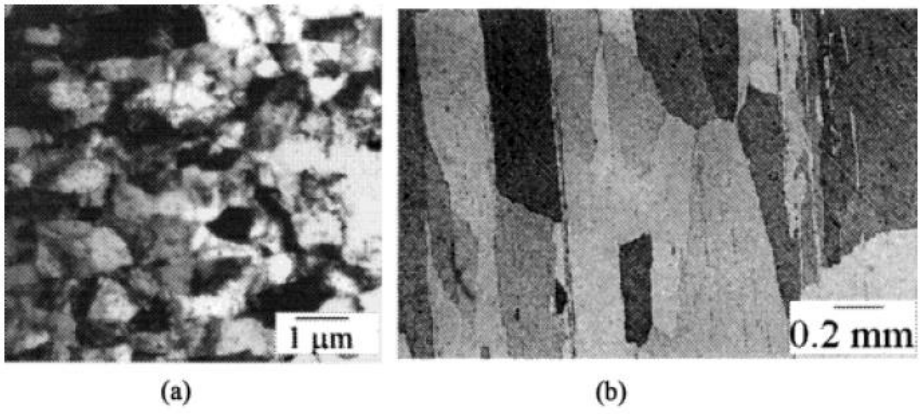

Figure 10 a) Transmission electron micrographs showing the sub-micrometer grain structure of mechanically alloyed and consolidated iron-based MA957 alloy, b) optical micrograph showing the coarse, columnar recrystallized grain structure resulting from annealing at 1400 °C. (5)

3.5 Recrystallization

Table 2 shows the hardness of various superalloys. As it can be seen from the Table, the alloys are very hard in the consolidated state. However, their fine grain structure needs to be modified if the primary requirement is creep resistance. This modification is done by recrystallization, which changes the fine grain structure to the coarse grain structure, and reduces the amount of grain surface per unit per volume by 2-3 orders of magnitude. (5)

Table 2 Vickers hardness for commercial alloys, before and after recrystallization.

Alloy	HV, before recrystallization	HV, after recrystallization
PM2000	400	290
MA957	400-410	230-240
MA956	350-390	225-245
MA956Sheet	410	250
PM1000	550	250
MA6000	645	500-520
MA760	720-790	500-515
MA758	405	214

It is also possible to obtain columnar grain structure from the alloys listed in Table 1. The width of these columnar grains can be hundreds of micrometers and their length can be as long as the sample length. Because of the particle alignment, the grains grow anisotropically during consolidation and heat treatments. It should be taken into the account that the limiting the grain size is obtained by pinning particles on the grains boundaries. Although the particle pinning has a great role in obtaining an anisotropic recrystallization microstructure, it is not the controlling factor of the scale of grain growth. This scale is controlled by the nucleation process. (7) (5)

Alloys with similar base elements recrystallize at lower temperatures (0.6 T_m) compared to the mechanically alloyed metals. The recrystallization temperature of the mechanically alloyed metals can reach temperatures around 0.9 T_m. Also, the mechanically alloyed metals contain more stored energy than normal metals (Table 3). There are several explanations that describe the recrystallization temperature (T_R). Nakagawa et al. (8) suggested that the high recrystallization temperature of nickel alloys is due to the γ'-precipitates. However, the recrystallization temperature is lower than the temperature needed to dissolve the γ'-precipitates. It has been also mentioned by Jongenburger (9) that the solute drag limits the grain boundary mobility unless the temperature is more than a specific value. In every situation, the solute drag is an inseparable feature of the commercial alloys, which are impure. This makes it hard to observe the true reasons for the high recrystallization temperature of mechanically alloyed metals. (5)

Table 3 Enthalpy of recrystallization (5)

Alloy	Stored energy (Jg^{-1})	Materials example	Stored energy (Jg^{-1})
MA957	≈1.0	Supersaturated solution	<1
MA956	0.4	Intermetallic compounds	<0.5
MA956Sheet	≈0.4	Amorphous solids	<0.5
MA6000	0.6	Compositionally modulated films	<0.1
MA760	1.0	Interphase dispersions	<0.1
MA758	0.3	Commercial mechanical alloys	<0.005

3.6 Grain structure and texture

Different types of grain sizes and structures can be achieved depending on the thermomechanical treatments. It should also be noticed that the measurements of the grain size are difficult due to the high level of anisotropy in grain sizes. Usually the grain aspect ratio (GAR) is between 5 and 10 and the grains can be several millimeters long. For instance in MA760 the GAR can vary from 21 to 40. (10)

The work done by Martin and Tekin (11) on the grain boundary structure of MA6000 and MA760 shows that no high angle boundaries are present in the structure. However, MA760 is more strongly textured than MA6000 (3), and in MA760 agglomerated γ' covers the low angle grain boundaries. The importance of these agglomerated γ' precipitates is during the high temperature fatigue crack growth, where they act as paths for crack propagation. (3)

The recrystallization treatments lead to a structure, which typically has a strong texture. The deformation history of the alloy has a strong impact on the texture as well. In some cases temperature gradients in the annealing zone and the dispersoid parameters (size, shape, distribution and dispersoid matrix interfacial strength) have an effect on the texture as well. Formation of the texture in the ODS alloys has not been studied much, so there are several unanswered questions regarding this matter including the effects of process parameters, different types of textures, and micro mechanisms of texture formation. (12)

4. Strengthening mechanisms

The strengthening mechanisms, which operate in ODS superalloys are solid-solution hardening, precipitation hardening, dispersion hardening, grain boundary hardening, strain hardening, and texture hardening. Above 900^{o}C, the strength of the materials is due to the dispersions, while at intermediate temperatures γ'-strengthening is the most powerful mechanism.

4.1 Precipitation hardening

When the limit of solubility for the matrix phase is reached, the second phase particles start to nucleate and grow. This is due to reaching the equilibrium condition and providing suitable thermal condition. Nucleation of precipitation strongly depends on the temperature. There is a small driving force for precipitation process to start close to the solvus temperature. This is in contrast with rapid diffusion kinetics. Likewise, precipitation process has a slow rate at temperatures well below T_s, too (solving temperature) and this is in contrast with having a large driving force for nucleation of second the phase at this range of temperature. The reason is that at this range of temperature the diffusion is limited. Thus there is an optimal range of temperatures for rapid precipitation, where both the driving force and diffusion rate are ideal for nucleation and growth. This can be seen in Figure 11.

The precipitation process can be described in three different stages, the incubation period, formation of second phase clusters, and particle growth. After the incubation period, clusters of the second phase particles form and the nucleation and growth of the second particles start. Growth of the second phase particles can either be homogeneous within the matrix grains or heterogeneous along the grain boundaries of the matrix grains. The nucleation proceeds along with the particle growth until an equilibrium volume fraction of the second phase particles is reached. Finally, aging will result in coarsening of the particles, and the larger particles will continue growing at the expense of smaller particles. This is due to the reduction of the interfacial area between the two phases. This process is called Ostwald ripening, and it is a diffusion process to lower the interfacial area.

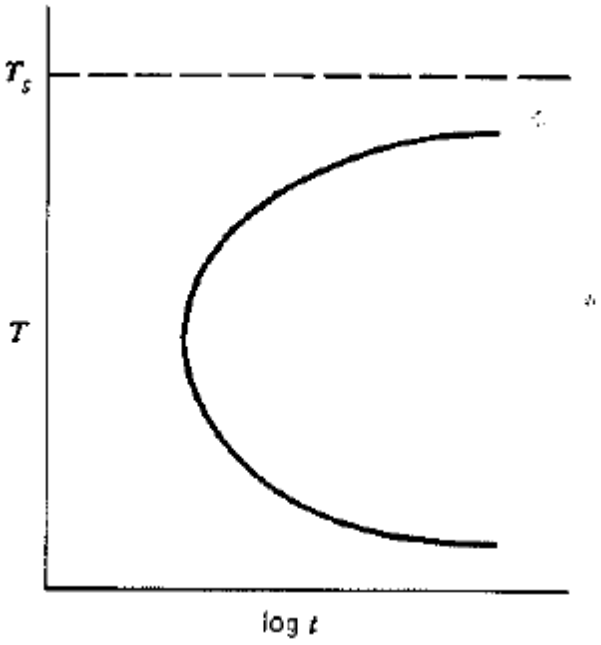

Figure 11 Precipitation rate as the function of temperatures (13 p. 138)

Normally the hardness and strength of the alloy increase with time and particle size, but may decrease with further aging, as can be seen in Figure 12.

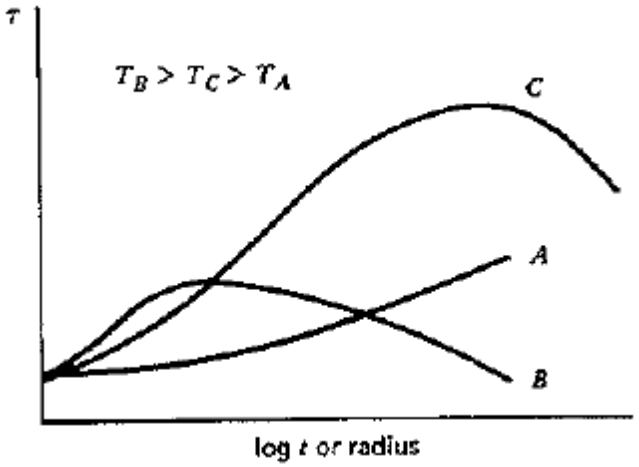

Figure 12 Schematic picture of an aging process at low (A), high (B), and intermediate (C) temperatures (13 p. 139)

The strength (τ) and the slope of the strength-time curve (dτ/dt) depend on four major factors; the volume fraction, distribution, the nature of precipitates, and the nature of the interphase boundary. The resistance to the dislocation motion increases with increasing the volume fraction of dislocation barriers (if other parameters remain constant) such as precipitates. The first two steps of aging increase the strength with time and/or particle dimensions (positive slope). On the other hand, long aging time and/or growth of large second phase particles (negative slope) is due to the Ostwald ripening (curves B and C in Figure 12). Depending on the structure of the second phase particles and the nature of the particle-matrix interface, the

dislocations may cut through the precipitates or avoid them. The motion of the dislocations at the interfaces between different phases depends on the level of coherency between the particles and the matrix. For a coherent interface, it can be expected that the dislocations pass easily through the interface from matrix to the precipitate. Yet at the same time the lattice misfit (created because of the different lattice parameters of the precipitate and the matrix) creates an elastic strain field around the coherent phase boundary. The shape of the particles in this area depends on the degree of misfit. When the misfit strain is small, the particles tend to gain a spherical shape. When these particles grow and/or a large misfit strain is developed, cuboidal particles are formed as in many of the nickel based superalloys (Figure13).

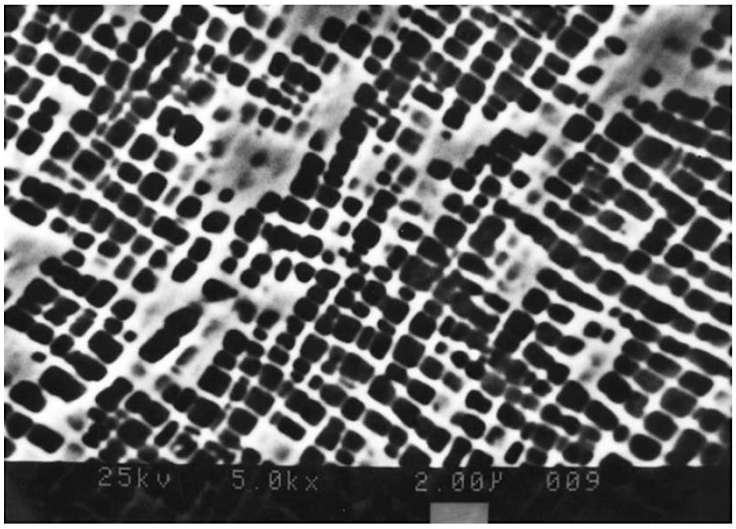

Figure 13 Cuboidal γ' particle in IN-100 superalloy (14)

As these small coherent particles start to grow, their interfaces become semi-coherent. The lattice misfit between the two phases is accommodated by the development of dislocations at the interface. At this point the misfit energy decreases significantly, whereas the surface energy increases by a great amount. As the aging process continues, coarser particles start to develop and interfaces between the two phases may completely break down and become incoherent. The surface energy at this stage increases whereas its strain field is essentially eliminated.

The reason for the change in the strength during the aging process is related to the interactions between the dislocations and the particles. These interactions themselves are different depending on whether the dislocations can cut through the particles or are they forced to loop around the particles. When particle cutting takes place, hardening depends on the elastic interactions between the dislocations and the precipitates. As it was mentioned before, the misfit between the matrix and the precipitate creates an elastic strain field. The strengthening related to the misfit can be estimated by:

$$\tau \sim G\varepsilon^{3/2}(rf)^{1/2} \qquad (14)$$

where ε is the misfit strain, r is the particle radius, f is the volume fraction of the precipitated second phase, and G is the shear modulus. For many nickel based superalloys the misfit strains are kept at the limit to maintain coherency for larger precipitates. Thus the strengthening part

of lattice misfit in these alloys is minor. On the other hand, low misfit strains lower the Ostwald ripening, which leads to higher creep resistance. (13 p. 141)

There is another situation if the dislocation cuts through the particle, in which energy storing mechanisms are involved. In this situation new interphase boundaries and anti-phase domain boundaries are created. When the dislocation cuts through the particle, it creates new interfacial area between and the matrix and the precipitates, which increases the overall energy of the lattice. As the interfacial energy of the coherent particles is small, this hardening mechanism has a low contribution to the overall strength of the alloy. However, if the precipitates have ordered lattice such as the γ' precipitates in nickel based superalloys, the motion of dislocations destroys the ordered structure of the precipitates and makes a large impact on the strengthening of the alloy. (13 p. 141)

In the case of high misfit strains, the interfaces are incoherent and dislocations are unable to cut through the precipitates. Instead, they loop around the precipitates as show in Figure 14. The stress necessary for the dislocation to loop around the precipitate can be calculated by:

$$\tau = \frac{Gb}{l} \tag{15}$$

where l is the distance between two precipitates, G is the shear modulus, and b is the Burgers vector. As more dislocations loop around the precipitates, the effective distance between the two precipitates decreases. For a specific volume fraction of the second phase particles, the distance between the particles increases as the precipitates grow larger and the stress necessary for the dislocation to loop around the precipitates decreases with increasing particle size. Dislocation bowing (Orowan mechanism) is not controlled by the nature of the precipitates as the cutting mechanism, but it is controlled by the distance between the two adjacent precipitates. Figure 15 shows the main mechanisms, which are involved in the strengthening of the alloy. It should be noted that the most homogeneous precipitates in the alloy systems are metastable with the exception of the γ' phase in the nickel based superalloys.

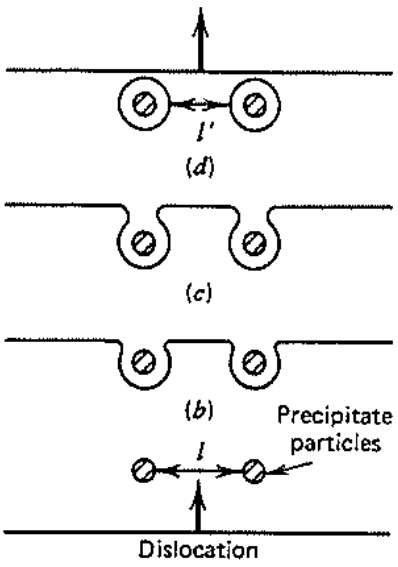

Figure 14 Dislocation looping around the particles (13)

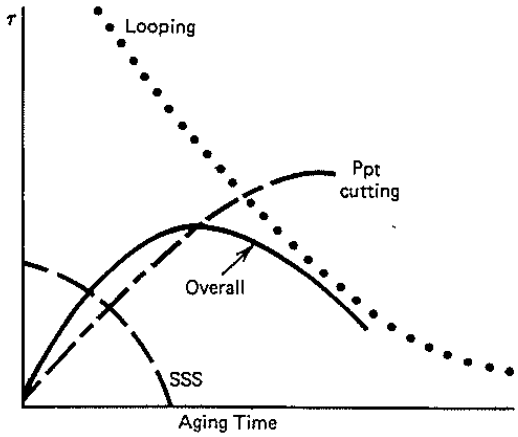

Figure 15 A schematic picture showing the role of the main hardening mechanisms in the overall hardening of the alloy (13)

4.2 Dispersion hardening

The basic principle of the dispersion hardening is based on the addition of the oxide particles that hinder dislocation motion. Adding ThO_2 to the nickel matrix will result in maintaining high strength at temperatures approaching the melting point of nickel. The strength of the alloy increases with increasing oxide volume fraction and decreasing particle spacing. (13 p. 143)

One of the first explanations for the interaction between the dislocations and the dispersions is based on the Orowan theory. In this model, when the dislocations meet non-shearable precipitates, they bypass it by a bowing-out mechanism, as shown in Figure 16. In order to complete this process, a critical shear stress is required, which leads to the formation of residual loop around the particle. Yet this theory was not successful to explain the behavior of

ODS alloys at high temperatures. Later on, Orowan's theory was replaced by theories based on localized climb of dislocations in the proximity of a dispersoid. The controlling factor for the deformation based on the climb theories is, of course, the climb of dislocations over particles. However, at low stresses and high temperatures this theory is not successful to explain the results. The experimental results show that there is an attractive interaction between the dislocations and the dispersoids. This attractive interaction was called departure side pinning (DSP) by Nardone et al. (15). DSP is schematically shown in Figure 17. From this Figure it can be seen that the dislocation is pinned on the departure side of the particle according to the direction of the shear stress. Bending configuration of the dislocation in Figure 17 indicates that the attractive interaction between the dislocation and the dispersoid prevents the further movement of the dislocation. As it was mentioned before, DSP takes place by localized climb of the dislocation over the particle and then pinning on the departure side. Based on this theory the threshold stress is the stress necessary for the dislocation to break away from the particle. It is also worth to mention that the climb of dislocations remains local only if the attractive forces exist between the dislocation and the particle. Without this attractive force, the curvature of the dislocation will lead to general climb. (3)

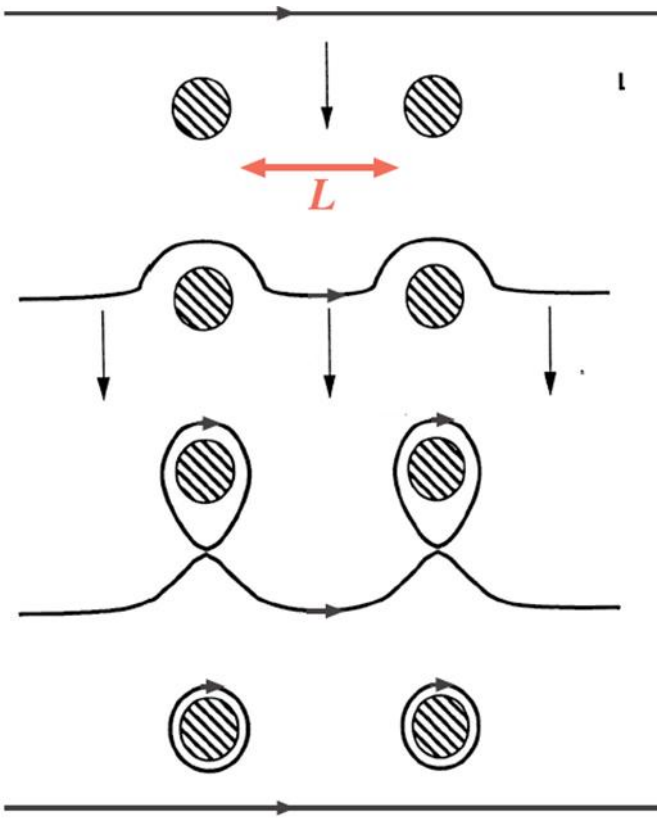

Figure 16 Schematic picture of the Orowan mechanism

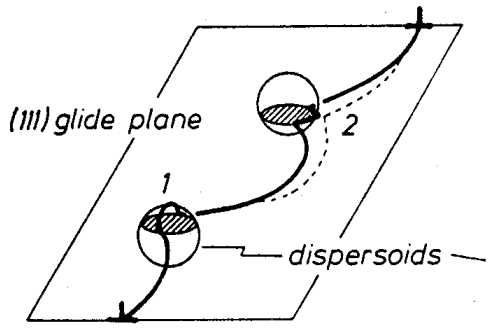

Figure 17 Schematic picture of dislocation climbing over dispersoid particles and the subsequent interfacial pinning (3)

Nardone et al. (15) suggested that the energy of the DPS can be because of several factors, which are: reduction in the dislocation line energy at the particle, segregation of the solutes on the interface of the particle and the matrix, and the surface energy effect. Elastic strain field of the dislocation and the dislocation core energy are the two main components of the dislocation line energy. An attractive interaction can be due to the large number of relative orientations between the particles and the matrix combined with the anisotropic nature of elastic constants. Work by Arzt and Wilkinson (16) shows that for materials with low volume fraction of particles (<13%), the strongest barrier for dislocations to bypass is the separation of the dislocation from the particle after the climb over the particle is completed.

4.3 Texture hardening and the effect of Grain boundaries

As it was mentioned before, a strong texture is normally developed during processing of the ODS alloys. Therefore, small samples may be similar to a single crystal more than a polycrystal. The strength of a single crystal can be calculated using the Schmid's Law, which takes into account the orientation of the single crystal:

$$\tau_C = R_P \, Cos\Phi \, Cos\lambda \tag{16}$$

where τ_C is the critical resolved shear stress, R_P is the yield strength in the loading direction, Φ is the angle between the normal of the slip plane and the tensile axis, λ is the angle between the slip direction and the tensile axis, and the product of ($Cos\Phi \, Cos\lambda$) is called the Schmid's Factor. (3)

However, in the polycrystalline alloys there are always grain boundaries and the orientation of the grains varies. The grain boundaries are effective barriers to the motion of dislocations. From the Hall-Patch Equation, the yield strength of a polycrystalline material can be calculated as:

$$\sigma_y = \sigma_i + k_y d^{-1/2} \tag{17}$$

where σ_y is the yield strength of the polycrystalline material, σ_i is the overall resistance of lattice to dislocation motion, k_y is the parameter, which measures the relative hardening contribution of grain boundaries, and d is the grain size. (13)

The number of dislocations, which can occupy the distance between the dislocation source and the grain boundary, can be calculated using Equation 18:

$$n = \frac{\alpha \tau_s d}{Gb} \tag{18}$$

where n is the number of dislocations in the pile-up, α is a constant, τ_s is the average resolved shear stress in the pile-up plane, d is grain diameter, G is the shear modulus, and b is the Burgers vector.

The stress acting on the lead dislocation is n times greater than τ_c. If the local stress reaches a critical value τ_s, the disabled dislocations will be able to glide over the grain boundary. Therefore:

$$\tau_c = n\tau_s = \frac{\alpha \tau_s^2 d}{Gb} \tag{19}$$

If the resolved shear stress τ_s is equal to the applied stress τ minus the frictional stress τ_i, the above Equation can be written as:

$$\tau_c = \frac{\alpha(\tau - \tau_i)^2 d}{Gb} \tag{20}$$

After rearrangement:

$$\tau = \tau_i + k_y d^{-1/2} \tag{21}$$

The above Equation is the shear stress form of Equation 14. σ_i may be separated into two components. First σ_{ST}, which is sensitive to the structure, and second σ_T, which is the temperature and strain rate sensitive component. Combining these two components, the yield strength of the material can be calculated by:

$$\sigma_y = \sigma_T + \sigma_{ST} + k_y d^{-1/2} \tag{22}$$

σ_T is related to the short-range effects (<10Å), σ_{ST} is related to the long-range stress field effects (100-1000Å), and $k_y y^{-1/2}$ is related to the very long-range structural size effects (>10^4Å). (13 pp. 129-130)

4.4 Solid solution strengthening

The basic idea of solid solution strengthening is to dissolve foreign atoms into a pure matrix. The effect of solute atoms on the strength of the material can be explained by different interactions, which occur between the solute atoms and dislocations. Adding solute atoms into the lattice causes distortions in the lattice, which can be felt energetically by the distortion fields of dislocations. Several local modifications in the lattice take place as the solute atoms are added into the lattice. These effects caused by the solute atoms are interrelated, as all of them are the result of electronic binding potentials. These different effects can be separated as dilatation, change of modulus, atomic ordering or segregation, chemical effects, and additional changes of the local electronic structure. (17).

The difference between the size of the matrix and solute atoms is characterized in an isotropic case by the size misfit parameter:

$$\delta = \frac{1}{a}\frac{da}{dc} \tag{23}$$

where a is the lattice constant and c is the concentration of solute atoms.

Dilatational effects result in elastic interactions and diffusive interactions. The most important part of the par-elastic interaction is due to the strain field of the dislocations and the strain of the locally modified lattice by the size misfit. This type of interactions are called par-elastic because of the distortion is already present without the dislocation's stress field. (17)

The change in modulus is due the modified binding forces around the foreign atom and it can be characterized by the modulus misfit parameters ɳ for the shear modulus and χ for the bulk modulus:

$$\eta = \frac{1}{G}\frac{dG}{dc} \tag{24}$$

$$\chi = \frac{1}{K}\frac{dK}{dc} \tag{25}$$

where G and K are the shear and bulk moduli. These moduli misfits cause elastic interactions because the strain field around the dislocation is proportional to the shear modulus.

Atomic ordering or segregation occurs according to the minimum of the configurational free enthalpy with negative or positive exchange energy, respectively. Therefore, the tendency to form larger obstacles over the single solute atom increases by increasing the concentration of the solute. Short range order or short range segregation causes stress fields, which produce frictional forces to the moving dislocations. This leads to the reduction of the mobility of dislocations. (17)

The effect of chemical interaction is the segregation of solute atoms into the stacking faults of the extended dislocations. This changes the width of the fault and pins the dislocations. This effect is stronger for the edge dislocations compared to the screw dislocations and plays an important role in the high temperature deformation. (17)

4.5 Strain (Work) hardening

Strain hardening is a result of increase in dislocation density, which leads to increasing dislocation-dislocation interactions and reducing the mobility of dislocations. As a result, higher stress is needed for further plastic deformation.

Examining the stress-strain response of a single crystal can be useful in defining the mechanisms of strain hardening of a metal crystal. Consider Figure 18, which shows the shear stress-shear strain curve of a single crystal initially oriented for single slip. Stage I is the region of easy glide, Stage II is the region of linear hardening, and Stage III is the region of dynamic recovery. (13 p. 124)

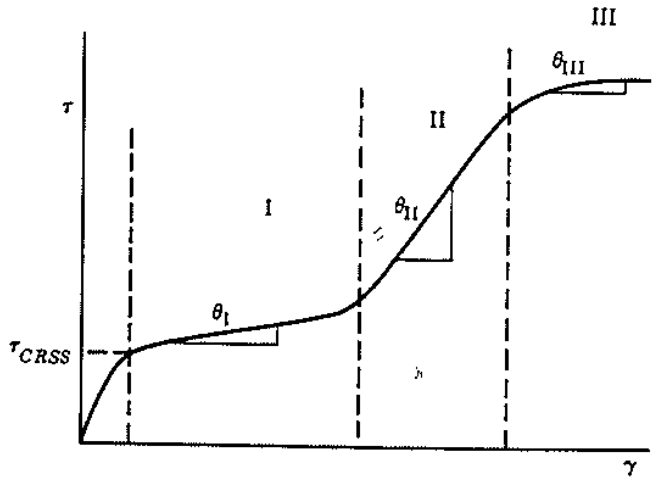

Figure 18 Shear stress-shear strain curve for a single slip oriented single crystal (13 p. 124)

Each region involves different aspects of plastic deformation for the single crystal. The scope of each region is dependent on different factors, such as test temperature, crystal purity, initial dislocation density, and initial crystal orientation. It is worth mentioning that the Stage III is similar to the behavior of a polycrystal of the same material.

The change in the strain hardening rate can be explained by dislocation interactions. A non-homogeneous distribution of low dislocation density can be seen in the crystal in stage I. Since the level of interactions between the dislocations is low, the dislocations can easily move along their slip planes, and the strain hardening rate θ_I is low. To obtain more plastic deformation, the necessary stress depends on the mean free dislocation spacing ($\bar{l}$):

$$\tau \propto \frac{Gb}{\bar{l}} \tag{26}$$

As the dislocation density is proportional to $1/\bar{l}^2$, Equation 26 can be written as:

$$\Delta\tau \propto Gb\,(\rho)^{1/2} \tag{27}$$

where ρ is dislocation density and Δτ is the shear stress needed to overcome the dislocation barrier. (13)

With increasing plastic deformation, ρ increases as well and leads to the decrease of the mean free dislocation spacing. It can be seen from Equations 26 and 27 that for further plastic

deformation the flow stress of the material increases. Stage III starts when dislocations are able to overcome the barriers around them by cross slip. The starting point of Stage III is affected by the stacking fault energy. For materials with high stacking fault energy, Stage III starts sooner compared to the materials with lower stacking fault energy. (13 p. 127)

When the density of dislocations is high (10^{11} to 10^{13} dislocations/cm^2), the structure remains stable only if the combination of stored strain energy (related to the dislocation sub-structure) and the thermal energy (related to the deformation temperature) remains below a certain level. If not, the microstructure becomes unstable and recovery, recrystallization, and grain growth start to take place leading to essentially strain free grains. The dislocation density in the new grains is much lower than before (10^4 to 10^6 dislocations/cm^2). Mechanical deformation, which at the given temperature causes recrystallization of the microstructure, is called hot working. On the other hand, if the microstructure at the given temperature is stable, the mechanical deformation is called cold working. The range of temperatures for hot working varies widely from one alloy to the other one. However, hot working temperatures can most often be found at temperatures close to one third of the absolute melting temperature of the alloy. (13 p. 128)

It is also worth considering the relation between the qualitative and quantitative aspects of the stress-strain response of single crystal and polycrystalline specimens of the same material. Early stages of deformation that appear for the single crystal could not be seen in the deformation of the polycrystalline specimen due to the large number of active slip systems. Therefore, the tensile stress-strain response of the polycrystalline material is similar only to the stage III of the single crystal material. In order to relate these two stress-strain curves, using the Schmid's Law it is possible to write:

$$\sigma = \frac{P}{A} = \tau \frac{1}{Cos\Phi Cos\lambda} = \tau M \tag{28}$$

where M = 1 / (cosΦcosλ)

In the case, for which the grains are randomly oriented in a polycrystalline sample, M would vary from one grain to the other one, so that an average orientation factor, $\bar{M}$, can be defined. Calculating $\bar{M}$ is not simple, but as the preferred combination of orientations is the one, for which the sum of the glide shears is minimized, it is possible to write:

$$\varepsilon = {}^{\gamma}/_{\bar{M}} \tag{29}$$

By combining Eq. 28 and 29, it can be shown that:

$$\frac{d\sigma}{d\varepsilon} = \bar{M}^2 \frac{d\tau}{d\gamma} \tag{30}$$

It can be seen from Eq. 30 that the strain hardening rate of a polycrystalline material is many times greater than that of the single crystal. (13 pp. 128-129)

5. High temperature behavior of nickel based superalloys

Nickel based superalloys have excellent properties that are tailor-made for high temperature applications. Table 4 shows typical physical properties of selected nickel based superalloys. It should be noted that the mechanical properties are strongly dependent on the microstructure. Mechanical properties of primary interest include tensile properties, creep, fatigue, and cyclic crack growth. Depending on the design of the final component, any of these properties can define the life limit of the material in service (18).

Table 4 Typical physical properties of some nickel based superalloys (18)

Property	Typical ranges
Density	7.7-9.0 g/cm^3
Melting Temperature	1320-1450^{o}C
Elastic modulus	Room Temp. 210GPa - 800^{o}C 160GPa
Thermal expansion	8-18 x 10^{-6} ^{o}C^{-1}
Thermal conductivity	Room Temp. 11W/m.k - 800^{o}C 22W/m.k

These alloys normally have rather high yield strength and high ultimate tensile strength. The yield strength is in the range of 900-1300 MPa and the ultimate tensile strength is in the range of 1200-1600 MPa at the room temperature. Figure 19 shows the temperature dependence of the yield strength for a single crystal and a powder disk alloy. (18)

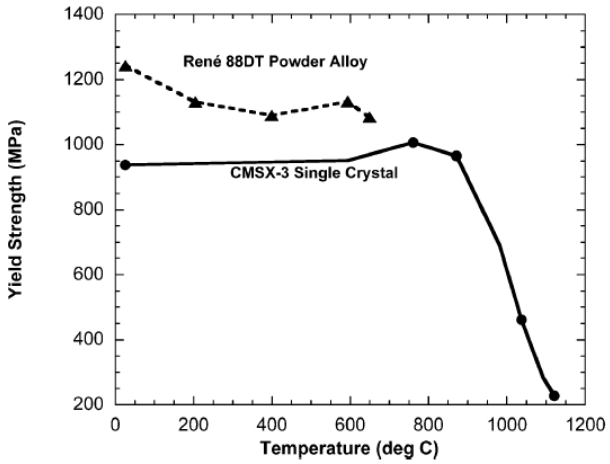

Figure 19 Yield strength as a function of temperature for two nickel based superalloys (18)

The rise in the yield strength of the single crystal as a function of temperature is due to the abnormal flow of the Ni_3Al (γ') phase. Figure 20 shows a rise in the critical resolved shear stress for some nickel based superalloys at intermediate temperatures. The reason for this rise is the deformation of the precipitates. It should be noted that the superalloys having two phases are stronger than both the matrix and the precipitates in the bulk form. (18)

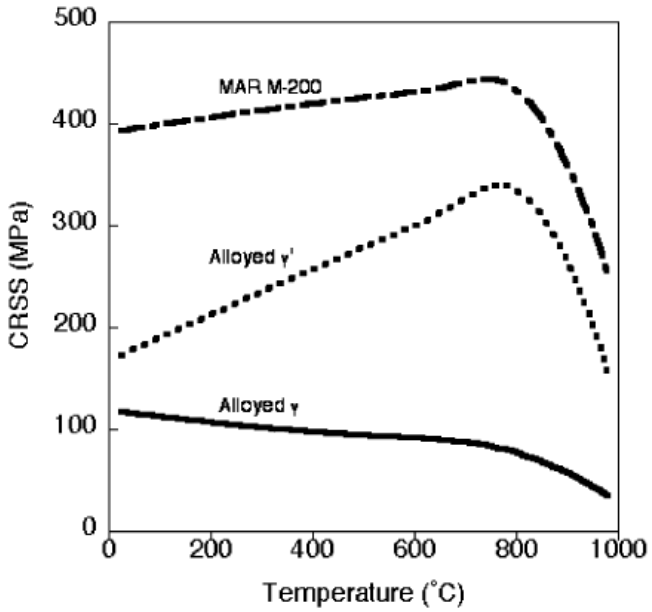

Figure 20 Critical resolved shear stress for MAR-M200 and its individual constituent phases (18)

Increase in the strength of the two-phase superalloys arises from the multiple interactions between the matrix and the precipitates. These interactions include the interactions between the dislocations and the precipitates (such as Orowan bowing). On the other hand, various heat treatments and processing at different temperatures lead to the population of precipitates with different sizes. For instance, three different types of population of precipitates for IN 100 can be seen in Figure 21. These three types are referred to as primary, secondary, and tertiary, in the order of decreasing size and precipitation temperature. The primary precipitates are not soluble in the late stages of processing, therefore, the precipitates start to grow and provide grain size strengthening. (18)

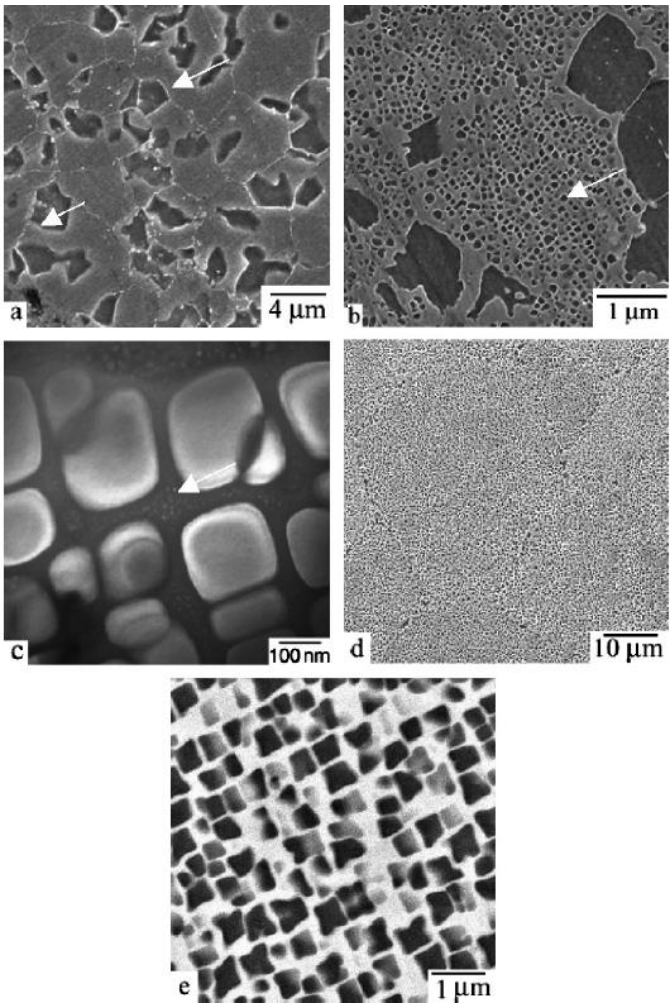

Figure 21 Population of precipitates in IN 100 (18)

In industrial superalloys, the Ni_3Al phase (γ') has a volume fraction between 40% to 70% and it is distributed randomly in the form of cuboidal particles in the γ matrix after the standard heat treatment. The high strength of these alloys is due to the anomalous yielding behavior of the γ' phase. The flow stress increases with increasing temperature until a maximum is reached at temperatures normally around 700°C. After this peak, the flow stress starts to decrease. Usually above 900°C, the initial cuboidal microstructure changes its morphology depending on the loading and the misfit of the lattice. The deformation mechanisms can be divided roughly into two groups. The first mechanism is active in the temperature range of 20°C to 700°C. In this region the particles are sheared by dislocation pairs as the plastic flow starts. This type of behavior is roughly similar to ideal plastic flow, and slip bands are formed. The second type of behavior can be seen at higher temperatures (above 700°C), where the deformation starts in the γ matrix. The matrix channels are filled with dislocation dipoles that create dislocation networks (Figure 22). Dislocations deposited on the grain boundaries create internal stress fields, which lead to kinematic hardening. This kinematic hardening is followed by softening and relaxation of these internal stresses by shearing of the γ' precipitates. There are three ways for the dislocations to pass the γ' precipitates. The first way is that the dislocations climb over the precipitates. The second way is by producing dislocation pairs, and the third way is the shearing of the γ' precipitates by super-lattice intrinsic stacking faults. The relaxation of the

internal stresses occurs by shearing of the γ' precipitates. After this stage, the dislocations are concentrated in the γ/γ' boundaries where, they create interfacial networks. (19)

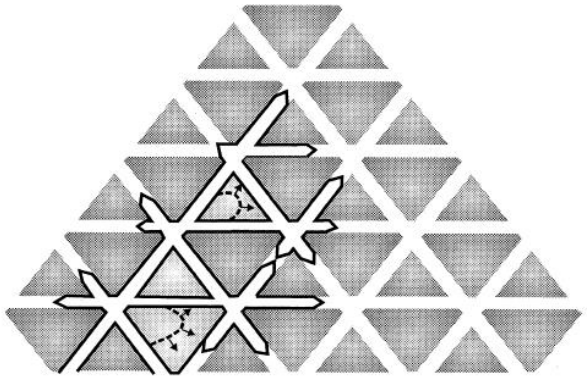

Figure 22 Arrangement of precipitates in an octahedral {111} plane. Dislocation dipoles are spreading in the channels and forming dislocation networks (19)

Work done by Feller et al. (20) show that there is clear difference between the low temperature and high temperature deformation of single crystals of nickel based superalloys. This difference, disregarding diffusion effects, is that at low temperatures the dislocation formation and expansion begins in the γ' phase, while at in the high temperatures it occurs in the matrix. Ideally the plastic behavior at low temperatures up to the temperature range of 600^{o}C to 700^{o}C is due to the formation of slip bands, which propagate through the material, and due to the restrictions of the single slip, which do not allow the strengthening by dislocations interactions. At higher temperatures (around 800^{o}C), by reducing the test time, which prevents the softening by climb, multiple slip is observed, which leads to continued hardening due to the establishment of dislocation networks. At higher temperatures (around 900^{o}C), closed loop dislocations still exist in the γ' phase at high strain rates. After the formation of dislocation networks in the γ/ γ' interfaces, softening occurs by shearing of the γ' phase and by diffusion controlled processes, such as dislocation climb. (20)

6. High strain rate testing

Strain rate is defined as the rate of change in strain over time. The measuring unit is s^{-1} and it can be defined by:

$$\dot{\varepsilon} = \frac{d\epsilon}{dt} \approx \frac{\Delta\varepsilon}{\Delta t} \quad (31)$$

Where Δε is the change in strain that occurs during the time Δt. High strain rate tests are performed to study the strain rate sensitivity of materials. Normal compression or tensile tests machines can provide the strain rates up to 1 s^{-1}. As the strain rate increases in these machines, oscillations in the measured force signals increase as well. Likewise, it is important to keep the load uniaxial and uniform during the whole test in high strain rate testing. The most common apparatus for this type of testing is the compression Split Hopkinson Pressure Bar (SHPB) device. Gray (21) explains the compression high strain rate testing using SHPB technique in details. The technique has been modified to operate also in tension and torsion loading as well.

6.1 Split Hokinson Pressure Bar

Figure 23 shows a schematic picture of the compressive Split Hopkinson Pressure Bar (22). There are various designs for the Compressive Split Hokinson Pressure Bar by different researchers, but the basic principle of the devices is the same. Figure 23 shows a typical design for a SHPB device. As it can be seen from the sketch, the specimen is sandwiched between the two pressure bars, called the incident (input) bar and the transmitter/transmitted (output) bar. A smaller bar, called the striker bar, is used to strike on the incident bar with a pre-calculated speed provided by the gas gun. As the striker hits the incident bar, the impact produces a stress wave into the incident bar, and the stress wave is partially transmitted and partially reflected at the surface of specimen. A third bar, called momentum trap bar, is sometimes used after the transmitter bar to trap the residual transmitted pulse, and to assure that the stress pulse does not reflect back to the transmitted bar as a wave of tension. The most important part in the device is the design of the bars which must remain in the elastic region during the test so that the data obtained from the gages on the bars can be used to calculate the stress and strain in the specimen. As measuring the wave in the bars plays an important role in the data analysis, it is quite important that the bars will be properly aligned so that the uniform stress state and uniaxial deformation can be achieved. (22 pp. 11-12) (23 p. 17)

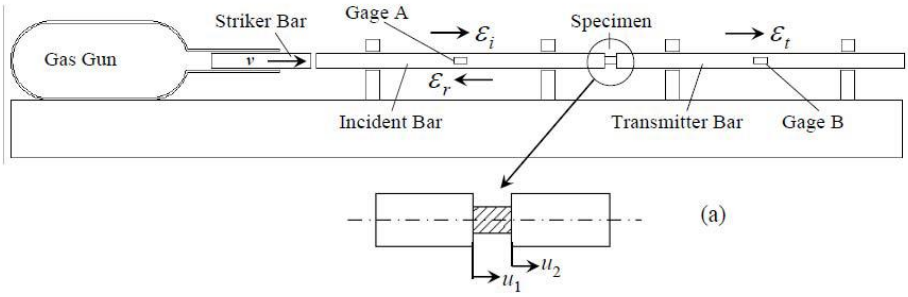

Figure 23 Schematic picture of a compressive Split Hokinson Pressure Bar (22)

Various factors influence the design, such as the length and diameter of the bars. According to Gray (21), one dimensional wave propagation should be achieved by choosing the right length and right diameter for the bars. According to the calculations, the ratio between the length and diameter (l/d) should be 10 or higher, yet this is not the only criterion. For separating the incident and reflected pulses clearly from one another, l/d ratio of 20 or more is usually necessary. In addition, the maximum strain rate, which can be achieved increases with decreasing the diameter of the bars. Besides, the total length of the bars has an effect on the total strain, which can be achieved in the specimens. As a guideline, to achieve more than 30% strain, l/d should be greater than 100. (22)

Also the selection of the bar material plays an important role in designing the apparatus. Since the aim of using the SHPB is to study the plastic behavior of materials, the bar material decides the limitations of the apparatus. As the bars must remain in the elastic region, the limit of the maximum stress attainable depends on the strength of the bar material. The most commonly used materials are high-strength steels and titanium and nickel alloys. Inconel alloys can withstand high temperatures so that specimens can be tested at temperatures up to 800 ^{o}C. The apparatus can also be designed so that the bars are not subjected to heat at all and only the specimen heated. In this case use of other materials for bars to run the test at high temperature is also possible. Although the above mentioned bars are the most common bars for testing metallic specimens, they are not so well suited for testing of low strength materials such as foams because of the large difference in the elastic moduli of the bars and the specimen, which decreases the signal-noise ratio and makes the measurements very challenging. (22)

6.2 Theory of the Split Hopkinson Pressure Bar

The principle of the Split Hopkinson Pressure Bar is based on the wave propagation in the bars and in the sample. Let the subscripts 1 and 2 stand for input and output bars. The wave Equations are given as:

$$\frac{\partial^2 u}{\partial x^2} = \frac{1}{c_b^2}\frac{\partial^2 u}{\partial t^2} \tag{32}$$

The displacements of the bar ends are given as:

$$u_1 = f(x - c_b t) + g(x + c_b t) = u_i + u_r \quad (33)$$

$$u_2 = h(x - c_t t) = u_t \quad (34)$$

where f, g, and h are functions describing the incident, reflected, and transmitted waves, respectively. C_b is the longitudinal wave speed in the bar and u_1 and u_2 are displacements in the incident and transmitter bars; u_i, u_r, and u_t are the incident, reflected, and transmitted displacement and the corresponding strains are ε_i, ε_r, and ε_t. Differentiating Equations 33 and 34 with respect to x yields:

$$\varepsilon_1 = \varepsilon_i + \varepsilon_r \quad (35)$$

$$\varepsilon_2 = \varepsilon_t \quad (36)$$

Differentiating Equations 33 and 34 with respect to time results in:

$$\dot{u}_1 = c_b(-f' + g') = c_b(-\varepsilon_i + \varepsilon_r) \quad (37)$$

where the prime sign denoted a derivative with respect to the terms in the brackets of Equation 33 for f and g respectively and:

$$\dot{u}_2 = -c_b \varepsilon_t \quad (38)$$

The forces F_1 and F_2 in the two bars can be written as:

$$F_1 = AE(\varepsilon_i + \varepsilon_r) \quad (39)$$

$$F_2 = AE(\varepsilon_t) \quad (40)$$

where A is the cross section of the bars and E is the elastic modulus of the bar material. According to the equilibrium assumption, these two forces should be equal, thus:

$$\varepsilon_t = \varepsilon_i + \varepsilon_r \quad (41)$$

Then the strain rate can be written as:

$$\dot{\varepsilon} = \frac{\dot{u}_1 - \dot{u}_2}{l_s} \quad (42)$$

Using Equations 41 and 42, the strain rate can be written as

$$\dot{\varepsilon} = \frac{2c_b \varepsilon_r}{l_s} \quad (43)$$

Using equation 40 and knowing that the force is the product of stress and area it is possible to write:

$$\sigma = \frac{AE\varepsilon_t}{A_s} \quad (44)$$

where A_s is the initial area of the specimen. Finally, the true stress and true strain in the specimen can be calculated using:

$$\sigma_{true} = \sigma_{eng}\left(1 + \varepsilon_{eng}\right) \tag{45}$$

$$\varepsilon_{true} = \ln(1 + \varepsilon_{eng}) \tag{46}$$

7. Taylor impact test

Taylor impact test was originally designed to analyze the dynamic yield strength of materials at moderate or high strain rates. When a cylindrical projectile strikes perpendicularly a flat rigid target, the stress at the impact surface quickly reaches the elastic limit, and the elastic compression wave travels through the target towards the rear end. The stress in this wave is equal or less to the elastic limit of the specimen. If the stress exceeds the elastic limit, the elastic wave is followed by a plastic wave. Once the compressive elastic wave reaches the rear end of the projectile, it reflects back as a tension wave. At this stage the velocity of the projectile in the part, which the reflected wave has not yet reached, is:

$$V = U - \frac{2\sigma_y}{\rho c} \tag{47}$$

where U is the original impact velocity, σ_y is the yield stress of the material, ρ is the density of the material, and c is the velocity of the elastic wave. (24)

The reflected elastic wave moves towards the impact end of the specimen until it reaches the incoming plastic wave from the target plate. In this plastic wave, the stress does not rise appreciably above the yield stress at any point near to the plastic-elastic boundary. On the other hand, the velocity of the plastic wave may be near to zero or at any other rate velocity of the plastic wave at the plastic-elastic boundary. When the reflected wave reaches the elastic-plastic boundary the part of the specimen, which is behind this boundary on the rear side, is stress-free and moves as a solid body with a velocity of U - $2\sigma_y/\rho c$. Thus it has the same conditions as at the time of the impact except that its velocity is U - $2\sigma_y/\rho c$ rather than U. The length of the part of the specimen that is behind the plastic-elastic boundary has a shorter length than L (24).

The length x of the specimen, which has not been plastically deformed yet depends on the velocity of the projectile, the speed of the elastic wave, and the velocity at which the elastic-plastic boundary moves away from the target plate. Assume that h is the distance from the elastic-plastic boundary to the target plate at any time, x is the length of the portion without plastic deformation, and u is the velocity of this rear portion. Formulas that describe the small changes in u, h, and x during the passage of the elastic wave from the plastic boundary and back to it are shown in Equations 48-51. It is worth mentioning that this movement of the elastic wave is a double passage and the duration for this double passage is:

$$dt = \frac{2x}{c} \tag{48}$$

so that:

$$dh = v\frac{2x}{c} \tag{49}$$

$$dx = -(u+v)\frac{2x}{c} \tag{50}$$

$$du = -\frac{2\sigma_y}{\rho c} \tag{51}$$

where v is the velocity of the plastic boundary. Eliminating c from Equations 48 to 51 will lead to:

$$\frac{dh}{dt} = v \tag{52}$$

$$\frac{dx}{dt} = -(u + v) \tag{53}$$

$$\frac{dx}{dt} = -\frac{2\sigma_y}{2x\rho} = -\frac{\sigma_y}{\rho x} \tag{54}$$

It should be noted that Equations 52- 54 can be derived only if the rear portions of the projectile are regarded as rigid. Equations 53 and 54 are not sufficient to determine the motion of the plastic-elastic boundary. In order to analyze the dynamics completely, there is a need to know all the intermediate states, which the projectile goes through between the impact and until it leaves the target plate. The simplest assumption about the stress-strain relation can be made to create a simple model of the phenomenon. It is assumed that the stress in the part of the projectile where the material is yielding is constant and equal to the yield stress σ_y. To assume constant stress, the radial inertia is neglected so the cross section is constant at any part of the specimen. Another assumption is that the material, which has passed through the plastic boundary, is brought to rest in a very short length. Figure 24 shows the simple theoretical model of a flat ended projectile fired at a speed of U at a flat target.

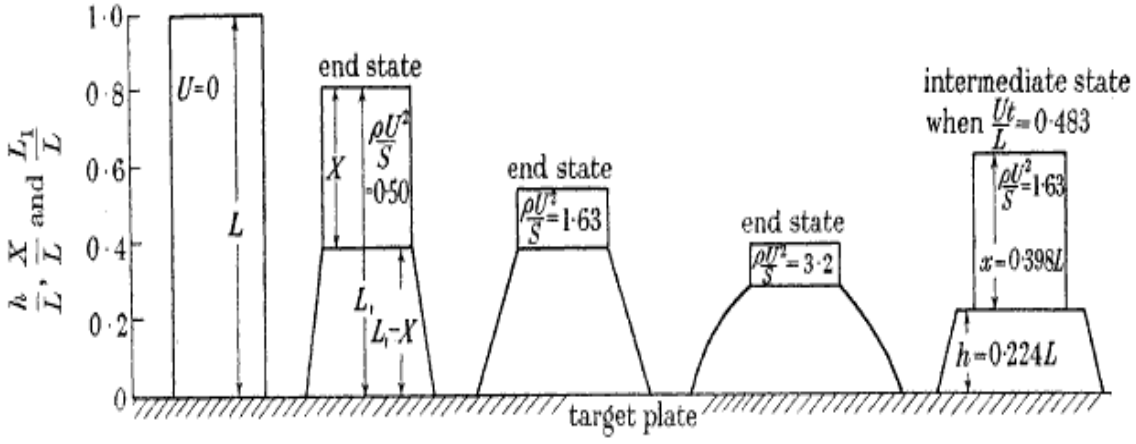

Figure 24 Simple theoretical model of a flat ended projectile fired at a speed of U at a flat target. In this Figure σ_y is shown by S (24)

The theoretical model at the moment when the rear end is still moving can be seen on the right hand side in Figure 24. Considering A_0 is the cross section of the projectile before the plastic deformation and A the cross section at the point where the material is brought to rest, it is possible to write:

$$A_0(u + v) = Av \tag{55}$$

If the stress on both sides of the thin region where the change in area occurs is equal to σ_y, the momentum equation will be:

$$\rho A_0(u+v) = \sigma_y(A - A_0) \tag{56}$$

The longitudinal strain caused by the compression at any point can be defined as:

$$e = 1 - \frac{A_0}{A} \tag{57}$$

By combining Equations 55-57 it is possible to write:

$$\frac{\rho u^2}{\sigma_y} = \frac{e^2}{1-e} \tag{58}$$

From Equations 53, 54, 55, and 57:

$$\frac{dx}{du} = \frac{(u+v)\rho x}{\sigma_y} = \frac{\rho u x}{\sigma_y e} \tag{59}$$

By integrating Equation 59:

$$log_e(x^2) = \int \frac{1}{e} d(\frac{e^e}{1-e}) = \frac{1}{1-e} - log_e(1-e) + constant \tag{60}$$

At the moment of impact x=L and e=e_1, and using Equation 58:

$$\frac{\rho U^2}{\sigma_y} = \frac{e_1^2}{1-e_1} \tag{61}$$

At the moment when the projectile is brought to rest, x=X and e=0. X is one of the measurable distances, and therefore:

$$log_e(\frac{x}{L})^2 = \frac{1}{1-e} - log_e - \frac{1}{1-e_1} + log_e(1-e_1) \tag{62}$$

and

$$log_e(\frac{X}{L})^2 = 1 - \frac{1}{1-e_1} + log_e(1-e_1) \tag{63}$$

Eliminating e_1 between Equations 61 and 63 gives X/L as a function of $\rho U^2/\sigma_y$. By using Equations 52 and 53, the shape of the projectile after the impact can be obtained:

$$\frac{dh}{dx} = \frac{-v}{u+v} = -1 + e \tag{64}$$

so that

$$h = -\int_L^x (1-e)dx \tag{65}$$

In order to develop a simple formula to estimate the yield point, one can assume that the plastic-elastic boundary moves at a uniform velocity from the impact plate to the final position. Another assumption is that the yield boundary defines the position where σ_y is reached. With these two assumptions is possible to determine the reduction of velocity of the rear part of the projectile. (24)

Considering C as the constant velocity of the plastic boundary and considering Equations 53 and 54:

$$\frac{du}{dx} = \frac{\sigma_y}{\rho x(u+c)} \tag{66}$$

After integration:

$$\frac{\sigma_y}{\rho} log_e\left(\frac{x}{L}\right) = \frac{1}{2}u^2 + Cu - \frac{1}{2}U^2 - CU \tag{67}$$

When x=X and u=0:

$$\frac{\sigma_y}{\rho} log_e\left(\frac{X}{L}\right) = -\frac{1}{2}U^2 - CU \tag{68}$$

In the case where the rear part of the projectile loses its velocity uniformly, C/U can be calculated simply by knowing the fact that the duration of deceleration, T, is equal to $(L_1\text{-}X)/C$ (where L_1 is the overall length of the projectile after the test) as well as also equal to $2(L\text{-}L_1)/U$ Thus:

$$\frac{C}{U} = \frac{\frac{1}{2}(L_1 - X)}{L - L_1} \tag{69}$$

So Equation 68 can be then written as:

$$\frac{\sigma_{y_1}}{\rho U^2} = \frac{(L-X)}{2(L-L_1)} \frac{1}{log_e(\frac{L}{X})} \tag{70}$$

where σ_{y1} is the yield stress instead of σ_y to differentiate it from the values calculated by more exact methods. As the true reduction of velocity is not constant, Equation 70 is only an approximation. The error due to this assumption can be estimated using the method presented by Taylor (24).

Since:

$$\frac{dx}{dt} = -(u + C) \tag{71}$$

Equation 67 may be written:

$$(\frac{dx}{dt})^2 = \frac{2\sigma_y}{\rho} log_e\left(\frac{x}{L}\right) + (U + C)^2 \tag{74}$$

and when u=0 and x=X:

$$\frac{2\sigma_y}{\rho} log_e\left(\frac{X}{L}\right) = C^2 - (U + C)^2 \tag{73}$$

Using $2\sigma_y/\rho = a^2$, $K = (U+C)/a$, $x_1 = x/L$, $t_1 = at/L$, and $T_1 = aT/L$, where T is the duration of the impact, a non-dimensional form of Equation 72 can be obtained:

$$\frac{dx_1}{dt_1} = \sqrt{(K^2 + log_e x_1} \tag{74}$$

so that:

$$T_1 = \int_1^{e-K^2} \frac{dx_1}{\sqrt{(K^2 + log_e x_1)}} \tag{75}$$

Using $K^2 + \log_e x_1 = z^2$,

$$T_1 = 2e^{-K^2} \int_{C/a}^{K} e^{z^2} dz \tag{76}$$

as the velocity of the elastic-plastic boundary is C, CT = L_1 – X. Inserting this in the non-dimensional form:

$$\frac{C}{a} T_1 = \frac{L_1}{L} - \frac{X}{L} \tag{77}$$

Then Equation 73 becomes:

$$log_e \frac{L}{X} = K^2 - \left(\frac{C}{a}\right)^2 \tag{78}$$

To calculate the error, the following correcting factor can be used:

$$\frac{\sigma_y}{\sigma_{y_1}} = \frac{L-L_1}{L-X} \frac{log_e(\frac{L}{X})}{(k-\frac{C}{a})^2} \tag{79}$$

7.1 Practical aspects of Taylor impact test

In order to demonstrate the application of the described Taylor method, one of the first attempts to find the dynamic yield stress of a paraffin wax will be described here. The cylindrical specimens with the length of 1.75 cm were cut from the bulk rod. After the test, the specimens became shorter but they did not fracture. The cylinders deformed at the impact end, but there was no sign of yielding on the other end of the specimens. The most significant property of the paraffin wax is that it is originally transparent, but as it passes through the yield point, it becomes opaque due to the micro-cracks that form during deformation. Thus this property makes it easy to locate the deformed region, which gone through yielding. The length of the transparent region was taken as X. The results of the tests are shown in Table 5. (24)

Table 5 The results of the Taylor impact tests on paraffin wax

Original Length L (cm)	Impact speed U (m/s)	Final length L_1 (cm)	Portion with plastic deformation X (cm)	Dynamic yield stress (σ_y)(MPa)
1.774	38.40	1.635	0.95	5.88
1.757	39.01	1.625	0.95	6.41
1.779	40.23	1.625	0.95	5.79

The measurements show that the specimens yield dynamically without suffering strain greater than 0.2% Comparing these results with the results obtained from mechanical tests at lower speeds, where the plastic deformation takes place, the strain rate can be defined by the terms that are experimentally measurable quantities. In this type of tests where the plastically distorted portion of the projectile can be accurately determined, it is possible to define the

rate of strain in the plastically deformed area only. Considering Equation 72, the mean rate of strain is U/2(L-X). As the reduction in length is equal to $L-L_1$, the total strain of the deformed part of the specimen is $(L-L_1) / (L-X)$, where L_1 is the length of the specimen at time t, and L is the original length of the specimen. If the deceleration is the same in each part of the specimen, then the time of deceleration will be $2(L-L_1)/U$, Therefore; the mean rate of strain (MRS) is:

$$MRS = \frac{(L-L_1)}{(L-X)} \frac{0.5U}{(L-L_1)} = \frac{0.5U}{(L-X)} \quad (80)$$

8. Experimental procedure

This Section describes the experimental procedure including the preparation of the Split Hopkinson Pressure Bar samples, the Taylor impact test samples, as well as the designing and building of the high temperature system for the Taylor impact test device.

8.1 Test materials and sample preparation

As the microstructure of the MA 760 has not been documented extensively, a short description of it is given below.

The grain structure of MA 760 is very coarse and the grains are elongated in the extrusion direction (Figure 25). The grain aspect ratio is around 15, and the texture in the extrusion direction is <110>, in the long transverse direction <111>, and in the short transvers direction <112>. γ' precipitates have the mean edge length of 0.50 µm, and they can be seen in the cuboidal shape having a volume fraction close to 50%. The mean spacing between the dispersoid particles is around 100 nm, and the average diameter of the dispersoids is close to 30 nm. Grain boundaries are primary low angle boundaries with agglomerated γ' (Figure 27).

Figure 25 Grain structure of MA 760 (25)

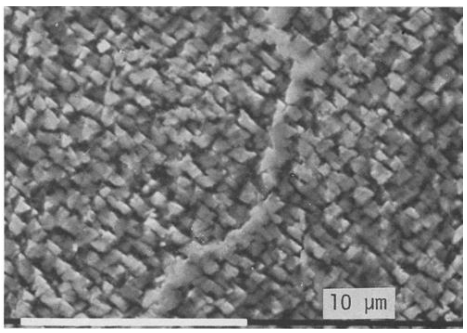

Figure 27 Grain boundary covered with agglomerated γ' (25)

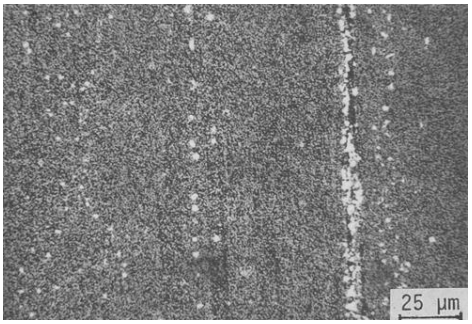

Figure 26 Stringers of inclusions in the extrusion direction (25)

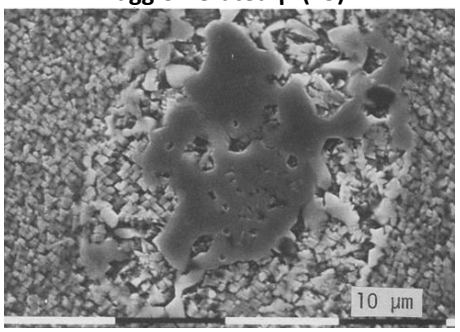

Figure 28 Typical inclusion with modified γ' structure surrounding it (25)

Nitride, carbide, and oxide inclusions can be observed as well as stringers of inclusions extending in the direction of extrusion (Figure 26). Inclusions usually change the composition of the surrounding matrix and the morphology of the γ' precipitates, as can be seen in Figure 28. (25)

Mechanically alloyed nickel based ODS superalloy MA 760 bars were produced with a rectangular cross section, of 20 mm x 60 mm. The bar was produced at Hereford Company, UK, and the final recrystallization heat treatment was carried out at Asea Brown Boveri, Badenm Switzerland. According to the birth certificate (3 p. 39) delivered by the company, the identification of the test material is as follows: mill batch No. EAR 2068/02, cast No. JBB 0161 and bar No. A9.3. Composition of the test material is presented in Table 6. The final heat treatment of the bar was annealing for 0.5h at 1100^{o}C, followed by furnace cooling at 60^{o}C/h to 600^{o}C, finally followed by uncontrolled furnace cooling.

The Split Hopkinson Pressure Bar samples were cut from the bar using EDM wire cutting. The samples had a cylindrical shape with the length of 6 mm and the diameter of 6 mm. Similarly, the Taylor impact test specimens were cut from the same bar with the length of 50 mm and the diameter of 6 mm. The 50 mm rods were finally cut in half using a rotating carbon disc cutter, producing samples with the length of 25 mm and the diameter of 6 mm.

Table 6 Composition of MA 760

Element	(wt%)
C	0.043
Si	0.04
Fe	1.02
Cr	19.66
Al	5.97
Mo	1.92
S	0.003
Zr	0.14
N	0.284
O	0.54
W	3.5
B	110 PPM
P	<0.005
Ni	Balanced
Y_2O_3	1.03

8.3 Split Hopkinson Pressure Bar test

The compression SHPB test system at the Department of Materials Science of Tampere University of Technology, which was used in this work, consists of three high strength steel (maraging steel) bars with the diameter of 22 mm and the length of 1200 mm or 1800 mm. The striker bars were made of the same material with the same diameter but with different lengths between 200 mm and 400 mm. The bars are put on four stanchions, supported by bearings, which make the alignment of the bars in the z- and y-axis possible. An air gun, which

provides the impact between the striker and the incident bar, consists of a barrel, a pressure container, and a pneumatic system with the ability of reloading the striker. Three optical IR-sensors are used to measure the velocity of the striker. These sensors also provide the trigger signal for the oscilloscope. There are two active strain gauges attached to the middle of the incident and transmitted bars. The signals of these strain gauges are amplified by a Kyowa CDV 700A series signal conditioner and recorded on a 12-bit 10MSample Yokogawa digital oscilloscope. All the functions of this device including loading of the striker, pressurizing, shooting, and reading the data from the oscilloscope to the computer are controlled by a computer. Figures 29 and 30 show the general overview and a schematic picture of the device. (23)

Figure 29 The compression SHPB equipment at the Department of Materials Science

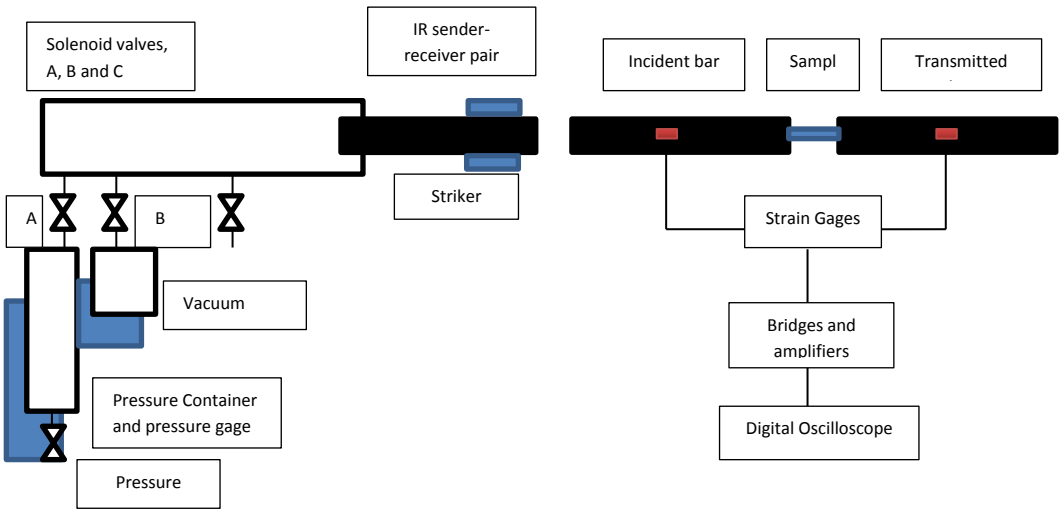

Figure 30 Schematic picture of the compression SHPB at the Department of Materials Science (23)

Figure 31 shows a schematic picture of the high temperature compression SHPB and its operating principle. A mechanical manipulator controls the bars and the sample, as the furnace is placed beside the bars to avoid the heating of the bars. The sample is placed in a ceramic wool ring, which is placed in a special specimen holder arm. This arm has the ability to pneumatically move back and forth between the centerline of the bars and the furnace. The first step to carry out the test is to move the sample inside the furnace. Enough time should be given to obtain homogeneous temperature over the sample. The second and third steps are to pull out the sample into the centerline of the bars rapidly and to shoot the striker. The second mechanical manipulator at the end of the momentum trap bar pushes the incident and transmitted bars and the sample into contact in a short time (around 50ms), just before the impact of the striker and the incident bar. This short contact time ensures that the temperature at the surfaces of the sample does not drop notably. (23 pp. 27-28)

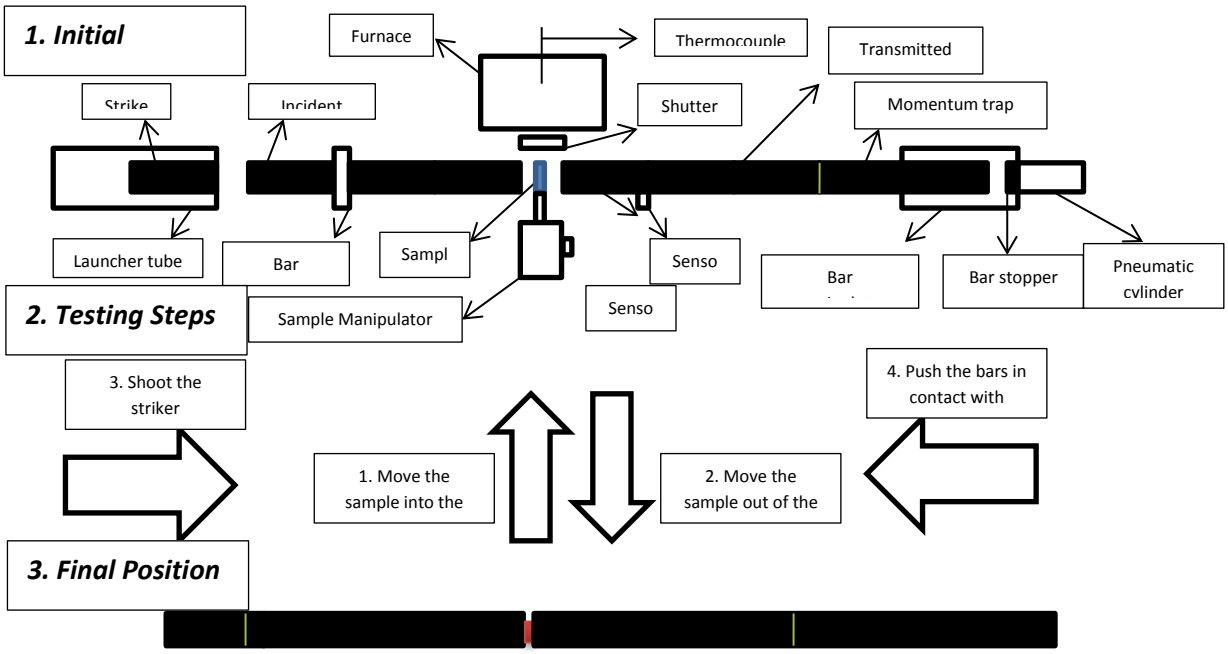

Figure 31 Schematic picture of the construction and testing steps of the high temperature compression test system

The Split Hopkinson Pressure bar tests were carried out at room temperature and at elevated temperatures. For the tests at room temperature the strain rate was the variable factor, while in the high temperature tests the strain rate was kept constant and the temperature was varied. Table 6 shows the tests parameters for the room temperature test. Each test was carried out three times to ensure repeatability of the results. Table 7 shows the test parameters for the high temperature tests.

Table 7 The room temperature tests

Test Variables	Temperature	Striker Length (cm)	Launch Pressure (bar)	Velocity of the Striker (m/s)	Target Strain Rate (1/s)
Test 1	Room Temp.	40	1.5	8.5	850
Test 2	Room Temp.	40	1.5	8.5	850
Test 3	Room Temp.	40	1.5	8.5	850
Test 4	Room Temp.	40	2.6	12.75	1600
Test 5	Room Temp.	40	2.6	12.75	1600
Test 6	Room Temp.	40	2.6	12.75	1600
Test 7	Room Temp.	20	3.8	23	3000
Test 8	Room Temp.	20	3.8	23	3000
Test 9	Room Temp.	20	3.8	23	3000

Table 8 The high temperature tests

Test Variables	Temperature (^oC)	Striker Length (cm)	Launch Pressure (bar)	Target Strain Rate (1/s)
Test 1	500	20	3.2	3000
Test 2	798	20	3.1	3000
Test 3	900	20	3	3000

8.4 High temperature Taylor impact test

A schematic picture of the high velocity particle impactor, which has been developed at the Department of Materials Science of Tampere University of Technology, is shown in Figure 32. This device has been used in this work to perform the Taylor impact tests. The speed of the projectile can vary roughly between 30 m/s and 200 m/s. The device has the ability to shoot projectiles with different shapes and compositions, such as metallic or ceramic balls and cylinders. The device consists of a smooth bore (firearm barrel without rifling) with the length of 550 mm and an internal diameter of 9 mm. Pressurized air is used to launch the projectile with the launch pressure ranging between 0.1 and 16 bars. The pressure is controlled and measured by a pressure gage, which is connected to the control computer. The target is placed at the distance of 1 m from the end of the barrel and can be tilted from 0^o to 90^o within a tolerance of 1^o. In order to have an accurate control of timing and repeatability of the tests, the device is completely computerized. In-house software has been developed to control the loading valve, pressure level in the tank, the shooting valve, the lighting, and video recording systems. The tests are recorded with a Memrecam fx k5 high speed camera, using frame rates up to 80.000 fps. (26)

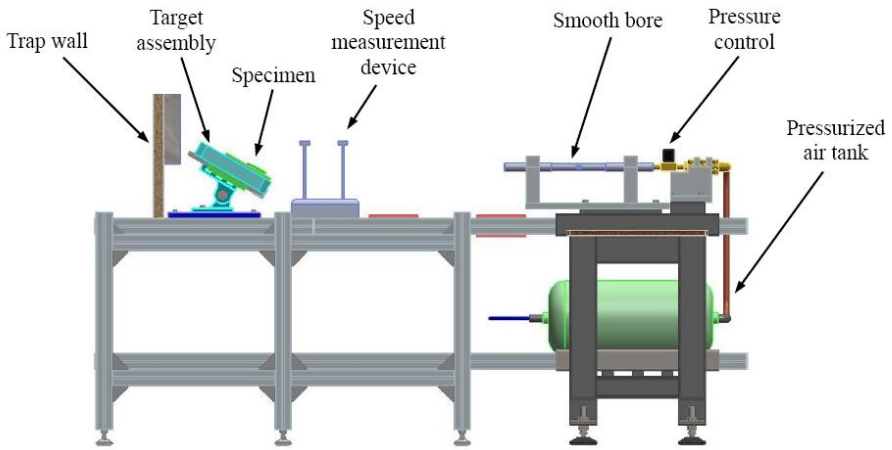

Figure 32 High velocity particle impactor at the Department of Materials Science (26)

8.5 High temperature Taylor impact tests

In order to perform the high temperature Taylor impact tests, some necessary modifications have been done to the device described above. Also a high temperature test system has been designed and built for this device. It should be noted that in this high temperature design, the target is shot against the stationary sample. This is exactly the opposite of the room temperature test, where the rigid wall is stationary and the specimen is shot against the wall. The first step in designing and building the high temperature apparatus for the Taylor impact tests was to design a stopper to stop and catch the high temperature sample and the projectile. Then the stopper was filled with ceramic wool to prevent the sample and the projectile from bouncing back from the back wall of the stopper, and also to prevent any further deformation of the sample after the initial impact. The stopper is shown in Figure 33.

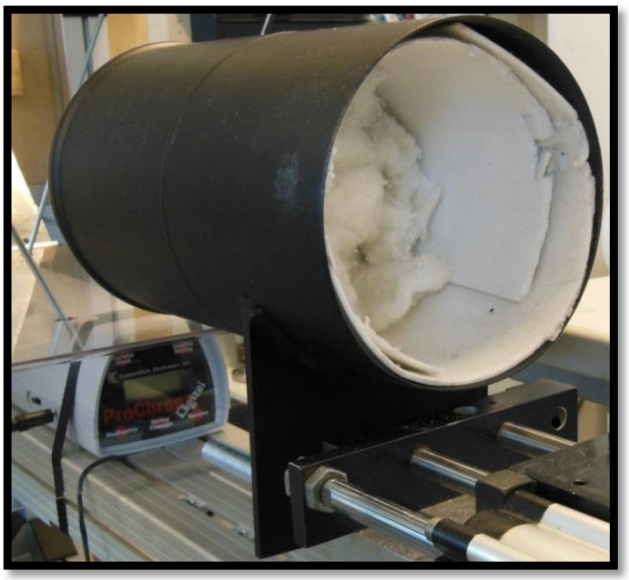

Figure 33 The stopper of the high temperature Taylor Impact test apparatus

In the first design, the sample holder was built from stainless steel. After running some preliminary experiments to check the efficiency of the device, it was observed that the sample holder heats up too much when it is placed inside the inductive heating coil. Therefore, the stainless steel sample holder was replaced with a non-conductive sample holder made from Teflon to prevent the increase of temperature in the sample holder. The Teflon sample holder is shown in Figure 34.

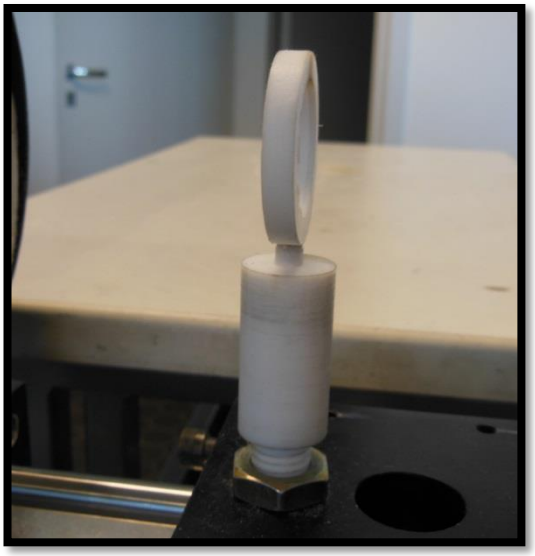

Figure 34 Teflon sample holder of the high temperature Taylor impact test apparatus

The sample holder was placed on a pneumatic slide to ease the alignment of the sample in the x and y directions. Also, the sample holder has the ability to move in the z axis and to rotate as well. Figure 35 shows the positioning of the stopper, the sample holder, and the gun with respect to each other.

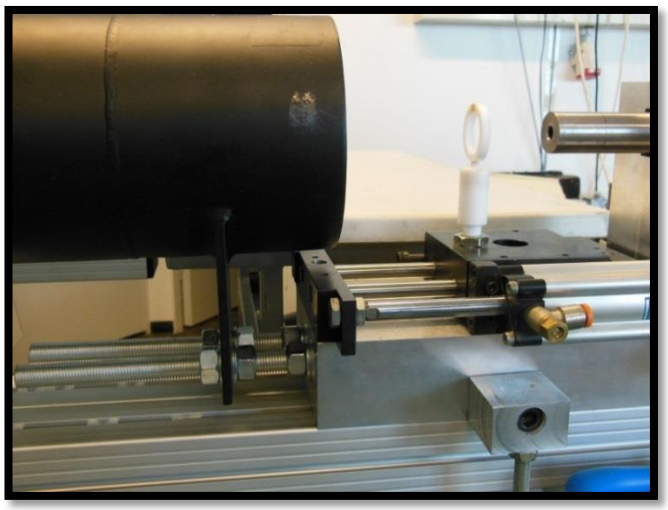

Figure 35 The stopper, the sample holder, and the gun of the high temperature Taylor impact test apparatus

To reach the required temperatures in the specimens, different designs of the induction coils were tested to obtain the most efficient heating conditions. After the preliminary experiments, the design shown in Figure 36 was selected.

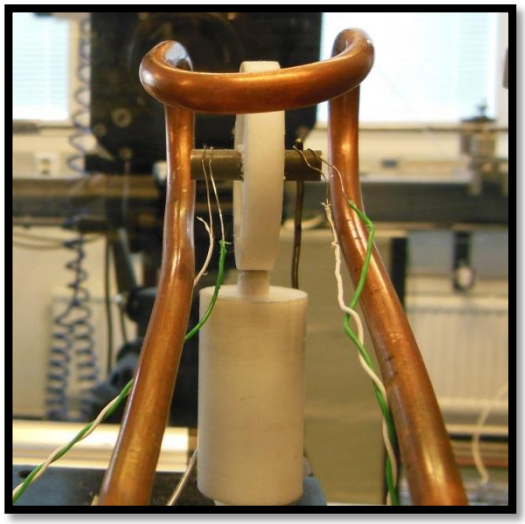

Figure 36 The design of the coil for the high temperature Taylor impact test apparatus

9. Results and discussion

This Chapter presents the results from the Split Hokinson Pressure Bar and Taylor impact tests.

9.1 Split Hopkinson Pressure Bar results

Before presenting and analyzing the results, it should be noted that MA 760 is highly textured, thus even small variation from the main texture direction can lead to completely different results. Also, the SHPB technique is a highly sensitive method. Small variations from the ideal situation (misalignment of the bars, putting the sample not exactly in the middle of the bars, and small scratches on the surfaces of the bars) may lead to different results. Also the geometry of the specimens has a huge impact on the test results. Unfortunately not all specimens were cut perfectly, and there were significant differences in the quality of the specimens. This was observed as extra scatter in the results.

Tests 1, 2, and 3 were carried out at the same conditions, and therefore they will be referred as test series 1. The same notation is used for tests 4, 5, and 6 (series 2), and tests 7, 8, and 9 (series 3). Figure 37 shows the true stress vs. true strain curves for tests 1, 2, and 3. As it can be seen, the curve obtained from the results of test 1 has a clearly different shape compared to the stress strain curves for tests 2 and 3. A closer look at Figure 37 shows that the yield behavior in test 1 is also different from that observed in tests 2 and 3. This is most likely because the ends of sample were more parallel after cutting than those of the two other samples. Similar behavior can be seen also in Figure 38, which shows the true stress vs. true strain curves for the tests 4, 5, and 6. Figure 39 shows the results for tests 7, 8, and 9. In this case the results match with each other much better than the curves in Figures 37 and 38.

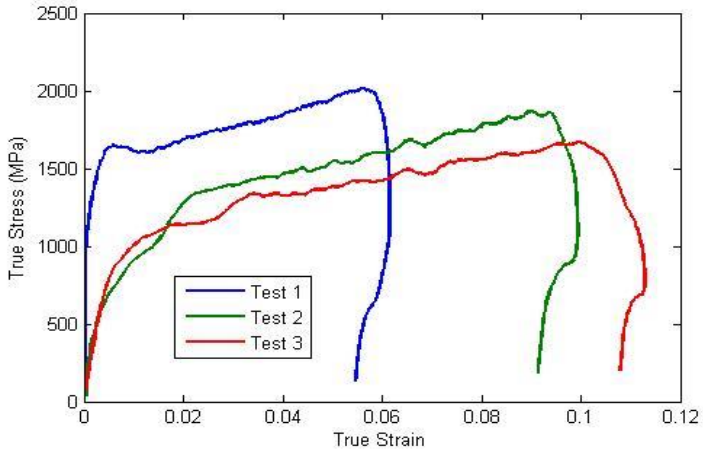

Figure 37 Room temperature true stress vs. true strain curves for tests 1 (550 s^{-1}), 2 (1400 s^{-1}), and 3 (1200 s^{-1}).

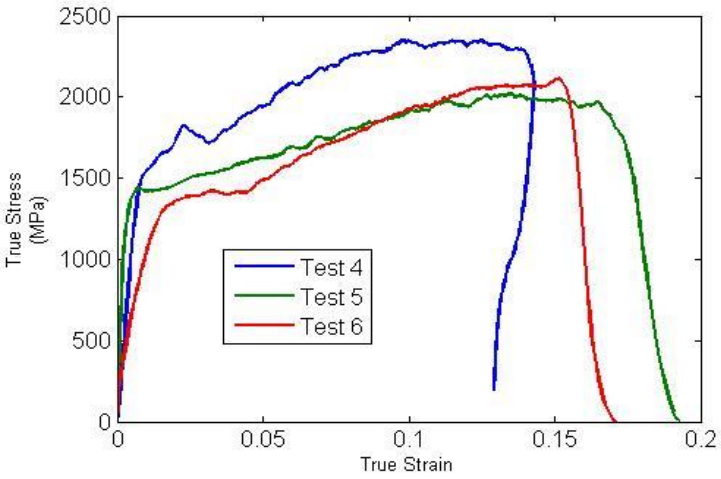

Figure 38 Room temperature true stress vs. true strain curves for tests 4 (1600 s^{-1}), 5 (1750 s^{-1}), and 6 (1600 s^{-1})

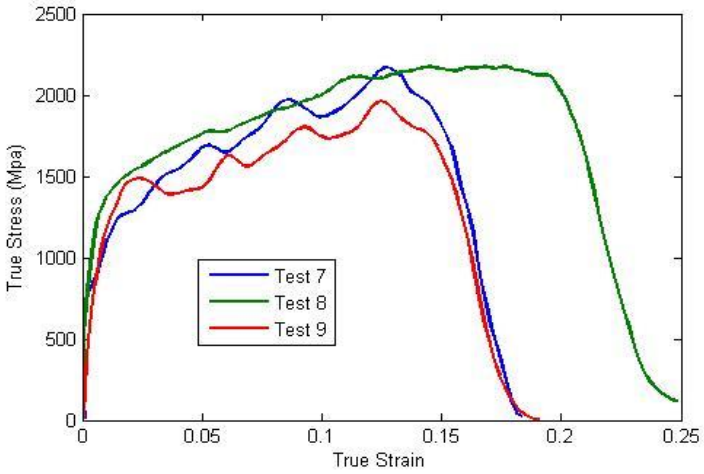

Figure 39 Room temperature true stress vs. true strain curves for the tests 7 (3300 s^{-1}), 8 (3350 s^{-1}), and 9 (3650 s^{-1})

Figure 40 shows the true stress vs. true strain curves obtained from the high temperature tests. Figure 41, in turn, shows the yield strength at room and elevated temperatures, indicating that the yield strength of the material increases slightly when the temperature is increased from room temperature to 500 ^{o}C. At temperatures above this the yield strength starts to decrease more strongly. These results match fairly well with results of the work done by Feller et al. (20) on a similar alloy. They also match with the result of the simulations done by Fedelich (19). Work done by Pollock and Tin (18) agrees with these results as well. It is worth to mention that the strength of the MA 760 increases with increasing temperature up to 700^{o}C, but after that the strength of the material decreases. This is due to the abnormal flow of the γ' phase below 700^{o}C, while above this temperature the deformation starts in the γ phase instead of γ' phase and the morphology of the precipitates changes around 900^{o}C.

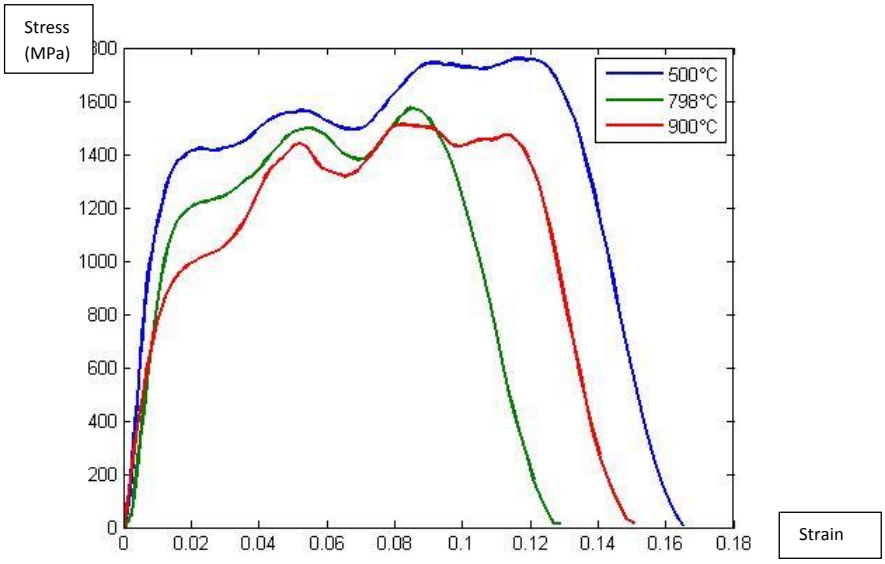

Figure 40 True stress vs. true strain curves at higher temperatures. At 500°C (3800 1/s), 798°C (3750 1/s), and 900°C (3450 1/s).

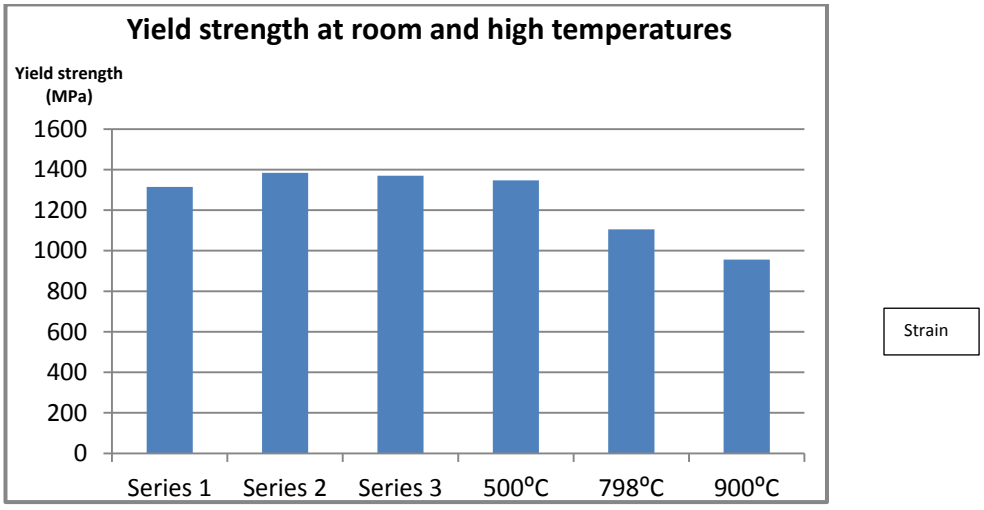

Figure 41 Yield strength at different temperatures

The yield strength of the specimens was calculated using the 0.2% proof stress rule. As the mechanical properties of MA 760 are not reported in any literature, to show the reliability of these results, the mechanical properties of MA 6000, which is a similar material to MA 760, were used for comparison. According to Niekov et al. (27 p. 392), the yield strength of MA 6000 at room temperature and at 871°C is 1284 MPa and 1156 MPa. Considering the differences between these two materials, the results obtained for MA 760 in this work are reasonable.

Figure 42 shows the maximum strains obtained for Series 1 and Series 2 tests and the fracture strain of Series 3, as well as the corresponding results of the high temperature tests. It should be noted that in the Series 1 and Series 2 tests the samples did not fracture, but the other specimens did. It should also be noted that the fracture is a local phenomenon. This means that the strain around the fracture point can be high, but the overall strain in the sample is still small. As it can be seen from Figure 42, the strains obtained in the tests change with increasing the strain rate between Series 1 and Series 2 but not so much between Series 2 and Series 3. On the other hand, by increasing the temperature to 500^{o}C where the strength of the material increases, the strain of the samples does not change by a considerable amount. A decrease in the strain of the sample can be seen in the 800^{o}C test, as the temperature increases, but at 900^{o}C the strain of the specimen again increases. This can be due to the morphological changes in the alloy. However, the changes in the fracture strains obtained in the Series 3 tests and in the high temperature tests are very small, and more tests should be performed to draw stronger conclusions on the high temperature high strain rate ductility of the material.

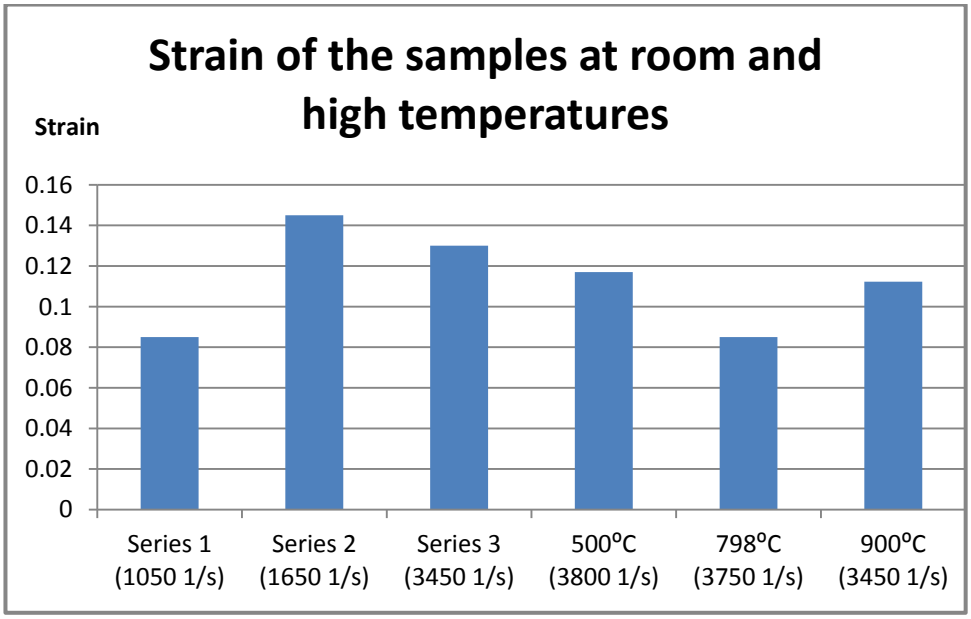

Figure 42 Maximum strain of the specimens at different temperatures. The strain in Series 3 and in the high temperature tests is the fracture strain, but the tests in Series 1 and 2 were finished before fracture of the specimen.

9.2 High temperature Taylor impact test results

Table 10 shows the data needed to calculate the yield strength and mean free strain of the specimens. The length of the deformed part of the specimen was measured using a thin metallic sheet, having a hole with the original diameter of the specimen. As only a small part of the specimen was deformed plastically, it is possible to slide the specimen through the hole until, at some point the specimen does not go through further because the deformed part has larger diameter than the non-deformed part. The density was calculated simply by dividing the weight over the volume.

Table 9 Data to calculate the mean free strain.

	Initial length of the sample (mm)	Final length of the sample (mm)	Density of the sample (g/cm^3)	Length of the plastically deformed region (mm)	Temperature (^oC)	Impact Speed (m/s)
Test 1	25.76	24.50	1.96	2.10	500	110
Test 2	24.56	25.34	1.96	2.15	500	180
Test 3	24.60	24.33	1.96	1.65	600	120
Test 4	24.59	24.40	1.96	1.34	600	180

Equation 80 was used to calculate the mean free strain rate. Figure 37 shows the mean free strain rate for each specimen.

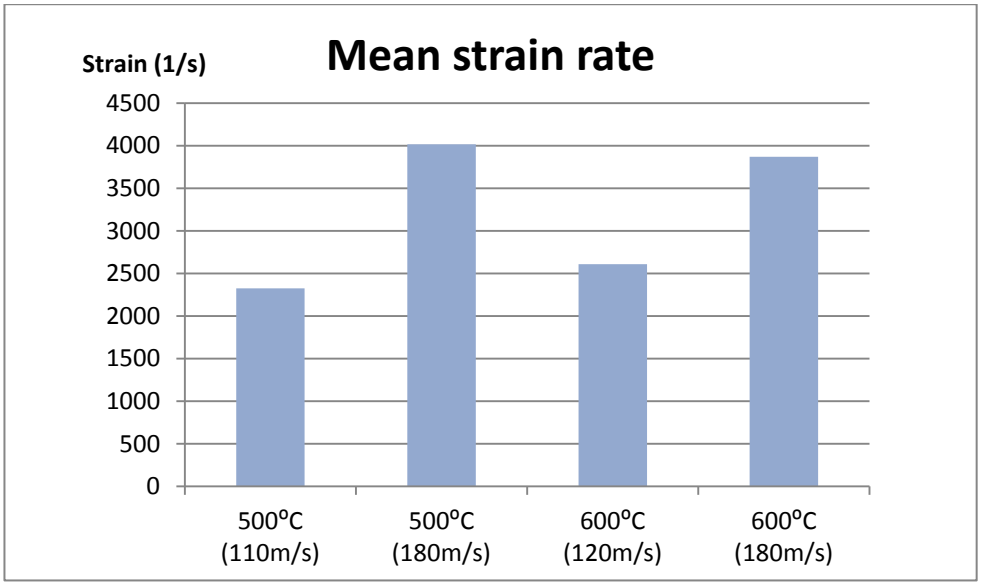

Figure 43 Strain rate in the specimen

The strain in each of the samples was calculated using both engineering strain equation and true strain equation. Figure 44 shows the results.

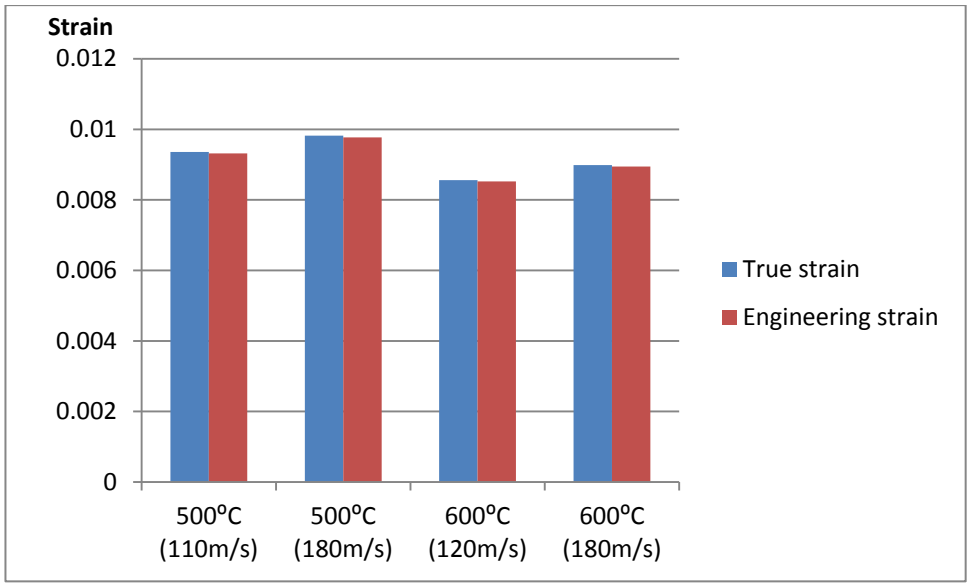

Figure 44 True strain and engineering strain for each sample

Figure 45 shows the dynamic yield strength of the samples used in the high temperature Taylor impact test. The difference between the yield strength and the dynamic yield strength is that the yield strength (static yield strength) is defined as the minimum stress to initiate flow when material is at rest. On the other hand, dynamic yield strength is the minimum stress to maintain flow in a dynamic loading situation (28). Equation 70 was used to calculate the dynamic yield strength.

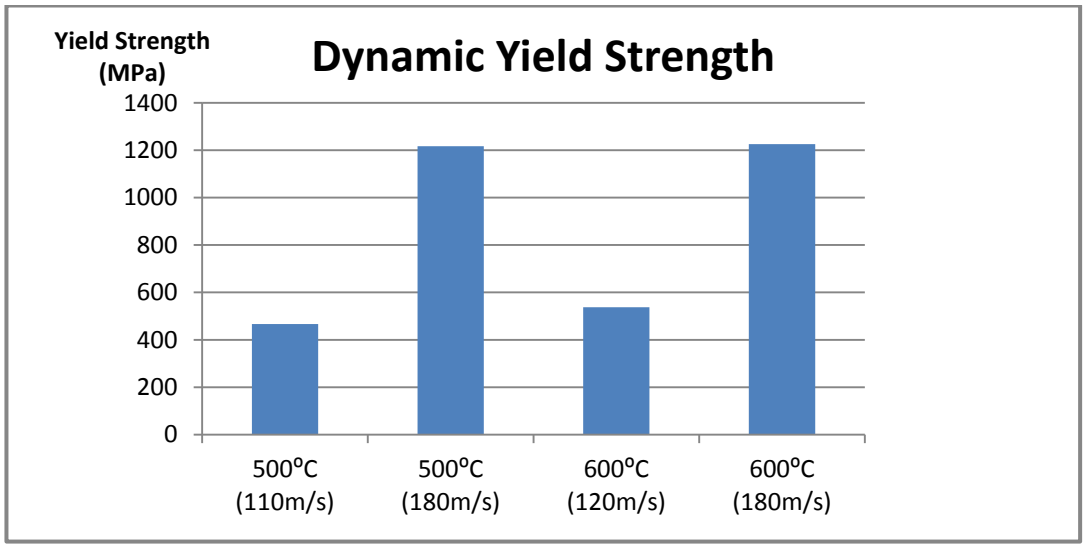

Figure 45 Dynamic yield strength obtained in the HT Taylor tests

The results show that by increasing the temperature the dynamic yield strength increases as well. It should be noted that the dynamic yield stress depends on the velocity of the projectile. Thus by increasing the speed of the projectile, the dynamic yield strength increases as well and vice versa. Comparison of the results obtained from the SHPB and high temperature Taylor impact tests in a quantitative way is not easy as the loading conditions in the two methods differ from one another. However, it is possible to compare the results qualitatively to see if the material shows similar behavior by changing a specific parameter. The behavior of the

material under dynamic loading matches with the results of the SHPB and also the results obtained by Fedelich (19), Feller et al., (20), and Pollock et al. (18).

There are some parts in the high temperature apparatus, which can be developed for further research. A more rigid coil can provide a stable range of the temperature over the sample. Also by improving the design of the coil according to the size of the sample makes it possible to reach higher temperatures. It is possible to design the coil in a way that makes it possible to record the moment of the impact with high speed cameras. In this way, it is possible to analyze the deformation of the material during the impact of the sample and projectile. The air coming out of the bore has a very high particle velocity, and therefore it can move the coil and the specimen. This should be minimized for more accurate testing. Replacing the ceramic wool ring by a more rigid material can assure that the specimen does not move before the test, and thus more accurate and better aligned impacts can be obtained.

The projectile used in this work was made out of aluminum alloy 7075, which has lower strength compare to the sample material (MA 760). Using projectiles, which are made out of the same material as the samples or of materials with even higher strength compared to the sample material can provide better results. The deformation of the samples in this work are small. Increasing the amount of strain in the sample can provide more accurate results. This can be done by for example using smaller specimens and higher impact velocities. If necessary, helium gas could be used instead of air for higher impact speeds. High speed camera could be used to monitor the deformation of the specimen during the impact. Also it is possible to use digital image correlation to techniques obtain the true 3D deformation of the surface of the specimen as a function of time.

.

10. Conclusions

The following conclusions can be made to summarize this thesis

1. A very thorough literature survey about the ODS superalloys was presented
2. A High temperature apparatus for Taylor impact test was designed, built, and successfully tested.
3. Compression tests were done using the Hopkinson Split Bar at room and at elevated temperatures. The strain rates ranged from 1200s^{-1} to 3800s^{-1} and the temperatures from room temperature to 900 °C.
4. The yield strength of the material in the high strain rate tests at room temperature was between 1112MPa and 1457MPa.
5. The strength of the material increases by increasing the temperature until 700 ^{o}C, then it starts to decrease.
6. Both temperature and strain rate have an effect on the maximum strain of the samples. By increasing the temperature until 800^{o}C, the strain decreases. Above this temperature it starts to increase again.
7. Although the strength of the material decreases at higher temperatures, the material is still very strong.
8. Several suggestions for further improving the high temperature Taylor test device were given:
    a. Positioning of the sample in the high temperature apparatus for Taylor impact test could be controlled by a computer.
    b. Replacing the ceramic ring wool by a more rigid material could prevent any movement of the sample prior to the impact.
    c. By improving the design of the coil, it should be possible to reach higher temperatures.
    d. High speed cameras could be used to analyze the deformation
    e. Use of stronger projectiles can assure better results.

Bibliography

1. **Smith, William Fortune.** *Structure and properties of engineering alloys.* s.l. : McGraw-Hill, 1993.

2. *The nature of the dispersoid in INCONEL alloy MA6000.* **G.B Schaffer, M. H. Loretto, R. E. Smallman, J. W. Brooks.** 1989, Journal of Materials Science, pp. 3261-3266.

3. **Hynnä, Antti.** *High temperature low cycle fatigue behavior of ODS superalloy MA 760.* Tampere : Tampere University of Technology Publication, 1994.

4. *Despersion strengthened superalloys by mechanical alloying.* **Benjamin, John S.** 1970, Metallurgical transactions, pp. 2943-2951.

5. *Manufacturing and microstructural evolution of mechanically alloyd oxide dispersion strengthened superalloys.* **Carlos Capdevia, Harry K. D. H. Bhadeshia.** 2001, Advanced engineering materials.

6. *Mechanical alloying.* **Benjamin, J. S.** 1976, Scientific American.

7. *The evolution of solutions: A thermodynamic analysis of mechanical alloying.* **A. Y. Badmos, H. K. D. H. Bhadeshia.** 1997, Metallurgical and materials transactions A, pp. 2189-2194.

8. *Abnormal Grain Growth of ODS Superalloys Enhanced by Boron Doping or Torsional Strain.* **Y.G. Nakagawa, H. Terashima, K. Mino.** Seven Springs Mountain Resort, Champion, Pennsylvania : The Society, 1988. pp. 81-89.

9. **Jongenburger, P.** *ODS superalloys for gas turbines.* Lausanne : Ecole Polythenique Federale de Lausanne, 1988.

10. *Cyclic deformation, holdtime creep and thermomechanical fatigue of an ODS superalloy.* **R. Joos, E. Arzt.** 1998, Z Metallkd, pp. 653-660.

11. **J. W. Martin, A. Tekin.** *COST 501-2, Project No. UK7, WP1 - ODS, Report No. 2.* Oxford : Oxford University Publication, 1990.

12. *Powder metallurgy of superalloys.* **R. F. Singer, G. H. Gessinger.** 1984, Metallurgical transactions, pp. 211-220.

13. **Hertzberg, Richard W.** *Deformation and fracture mechanics of engineering materials.* s.l. : JOHN WILEY & SONS, INC., 1996.

14. *Review progress in Ostwald ripening theories and their applications to the γ'-precipitates in nicke-base superalloys.* **Baldan, A.** 2002, Journal of materials science, pp. 2379-2405.

15. *The threshold stress and departure side pinning of dislocations by dispersoids.* **V.C. Nardone, D.E. Matejczyk, J.K. Tien.** 1984, Acta metall, pp. 1509-1517.

16. *Threshhold stresses for dislocation climb over hard particle: the effect of attractive interaction.* **E. Arzt, D.S. Wilkinson.** 1986, Acta metallurgica, pp. 1839-1898.

17. *Solid solution strengthening.* **H. Neuhäuser, C. Schewink.** Dresden : Dresden technical university, 2006, Materials Science and Technology.

18. *Nickel-based superalloys for advanced turbine engines: chemistry, microstructure, and properties.* **Tresa M. Pollock, Sammy Tin.** 2006, Jounal of Propulsion and Power, pp. 360-378.

19. *A microstructure based constitutive model for the mechanical behavior at high temperatures of nickel-base single crystal superalloys.* **Fedelich, B.** 1999, Computational materials science, pp. 248-258.

20. *Temperature dependence of deformation mechanisms in a single crystal nickel-base alloy with high volume fraction of γ' phase.* **M. Feller-Kniepmeier, T Link, I Poschmann, G. Scheunemann-Frerker, C. Schulze.** 1996, Acta Materialia, pp. 2397-2407.

21. **III, G.T. Gray.** *ASM Handbook Vol. 08 : Mechanical Testing and Evaluation.* [ed.] D. Medlin H. Kuhn. Material parks, Ohio : ASM Int., 2000.

22. **Yatnalkar, R. S.** *Experimental investigation of plastic deformation of Ti-6Al-4V under various loading consitions.* Columbus : Ohio State University, 2010.

23. **Hokka, M.** *Effects of strain rate and temperature on the mechanical behavior of advanced high strength steel.* Tampere : Tampere University of Technology Publication, 2008.

24. *The use of flat-ended projectiles for determining dynamic yield stress. I. Theoritical considerations.* **Taylor, G.** 1948, Proceedings of the Royal Society of London. Series A, Mathematical and Physical Sciences, pp. 289-299.

25. *High -temperature low-cycle fatigue behavior of superalloys MA 760.* **A. Hynnä, V.T. Kuokkala, J. Laurila, P. Kettunen.** 1993, Materials Engineering and Performance, pp. 531-536.

26. *High velocity particle impactor - modeling and experimental verification of impact wear test.* **M. Apostol, V. T. Kuokkala, A. Laukkanen, K. Holmberg, R. Waudby, M. Lindroos.** Torino : s.n., 2013. World Tribology Congress.

27. **O. D. Neikov, S. Naboychenko, I. B. Mourachova, V. G. Gopienko, I. V. Frishberg, D. V. Lotsk.** *Handbook of non-ferrous metal powders.* s.l. : Elsevier, 2008.

28. *Selecting admixtures to achienve application-required rheology.* **E. Koehler, A. Jeknavorian, S. Klaus.** Montreal : Springer, 2010. Design, Production and Placement of Self-Consolidating Concrete. pp. 79-88.

29. **Reed, Roger C.** *Superalloys: Fundamentals and Applications.* s.l. : Cambridge Publications, 2006.

30. **James Deane Patterson, Bernard C. Bailey.** *Solid-State physics: Introduction to the theory.* s.l. : Springer, 2010.

31. *Dislocation behavior in fatigue II. Friction stress and back stress as inferred from an analusis of hystersis loops.* **Kuhlmann-Wilsdorf, D.** 1979, Materials science and engineering, pp. 111-120.